Check for updates

Inhibition of monoamine oxidase by fluorobenzyloxy chalcone derivatives

Sachithra Thazhathuveedu Sudevan,†[a] Jong Min Oh,†[b] Prabitha Prabhakaran,[c] Mohamed A. Abdelgawad,[d] Mohammed M. Ghoneim,[e] Rasha Hamed Al-Serwi,[f] Hoon Kim*[b] and Bijo Mathew ✩ *[a]

Inhibition of monoamine oxidase-B (MAO-B) decelerates the breakdown of dopamine in the brain, consequently augmenting dopaminergic neurotransmission, which is a critical pathway for ameliorating motor symptomatology of Parkinson's disease (PD). Chalcones are widely recognized as the lead inhibitors of MAO-B and hold significant therapeutic value for PD. Inspired by safinamide's pharmacophoric features, the study focuses on designing, synthesizing, and evaluating a novel series of fluorinated benzyloxy chalcone derivatives as selective MAO-B inhibitors. Thirteen fluorobenzyloxy chalcone derivatives were synthesized and evaluated for their inhibition of monoamine oxidase (MAO). All compounds showed better inhibition of MAO-B than of MAO-A. Compound (*E*)1-(4-bromophenyl)-3-(2-((3-fluorobenzyl)oxy)phenyl)prop-2-en-1-one (**FBZ13**) most potently inhibited MAO-B with an IC_{50} value of 0.0053 μM, followed by (*E*)3-(2-((3-fluorobenzyl)oxy)phenyl)-1-(thiophen-2-yl)prop-2-en-1-one (**FBZ6**) (IC_{50} = 0.023 μM). The IC_{50} value of **FBZ13** was 4.0 times lower than that of reference drug safinamide. All compounds showed weak MAO-A inhibition, **FBZ13** and **FBZ6** displayed exceptionally high selectivity for MAO-B. Kinetic studies confirmed that these two compounds function as competitive and reversible MAO-B inhibitors. Additionally, PAMPA results indicated excellent membrane permeability and CNS bioavailability for **FBZ13** and **FBZ6**, highlighting their promise as central nervous system-active agents. *In vitro* antioxidant assays evaluated the activities of enzymes (SOD, CAT, GSH, and GPx) in human neuroblastoma cells exposed to lipopolysaccharide (LPS). Treatment with compounds **FBZ6** and **FBZ13** (10 μM each) significantly enhanced enzyme activities, mitigating LPS-induced oxidative stress. Lead compounds were stabilized in protein–ligand complexes by the π−π stacking, which enabled them to bind to the active site of hMAO-B effectively. These results suggest that **FBZ6** and **FBZ13** are potent reversible selective MAO-B inhibitors, and they can be used as potential agents for the treatment of neurological disorders such as Alzheimer's diseases and PD.

1 Introduction

Parkinson's disease (PD) is a progressive neurodegenerative disorder primarily affecting the dopaminergic neurons in the substantia nigra pars compacta, resulting in a substantial

decline of dopamine levels in the striatum. This neurochemical deficit gives rise to the cardinal motor symptoms of PD, including bradykinesia, resting tremor, rigidity, and postural instability. Non-motor manifestations such as cognitive impairment, depression, sleep disturbances, and autonomic dysfunction are also common and contribute markedly to the reduced quality of life in PD patients.[1–4] The multifactorial etiology of PD encompasses genetic susceptibility, environmental triggers, and ageing-related oxidative and mitochondrial stress.[5] Despite major advances in symptomatic management, there remains no curative therapy for PD. Levodopa-based dopamine replacement therapy continues to be the clinical gold standard, often administered with a peripheral decarboxylase inhibitor such as carbidopa to optimize central dopamine availability.[6] However, long-term levodopa administration frequently leads to complications, including motor fluctuations and dyskinesias, that compromise sustained efficacy.[7] Consequently, adjunctive approaches such as dopamine

[a]*Department of Pharmaceutical Chemistry, Amrita School of Pharmacy, Amrita Vishwa Vidyapeetham, AIMS Health Sciences Campus, Kochi 682 041, India. E-mail: bijomathew@aims.amrita.edu; bijovilaventgu@gmail.com*

[b]*Department of Pharmacy, College of Pharmacy, Sunchon National University, Suncheon 57922, Republic of Korea. E-mail: hoon@sunchon.ac.kr*

[c]*Department of Pharmaceutical Chemistry, JSS College of Pharmacy, JSS Academy of Higher Education and Research, Mysuru 570015, India*

[d]*Department of Pharmaceutical Chemistry, College of Pharmacy, Jouf University, Sakaka 72388, Saudi Arabia*

[e]*Department of Pharmacy Practice, College of Pharmacy, AlMaarefa University, Ad Diriyah, Riyadh, 13713, Saudi Arabia*

[f]*Department of Basic Dental Sciences, College of Dentistry, Princess Nourah bint Abdulrahman University, P.O. Box 84428, Riyadh 11671, Saudi Arabia*

† Authors contributed equally.

agonists, catechol-*O*-methyltransferase (COMT) inhibitors, and monoamine oxidase-B (MAO-B) inhibitors have been adopted to enhance therapeutic outcomes.[8,9]

MAO-B inhibitors, including selegiline and rasagiline, are clinically established agents that selectively block dopamine catabolism in the brain, thereby prolonging dopaminergic signaling and mitigating motor symptoms.[10,11] Chalcones, belonging to the 1,3-diaryl-2-propen-1-one class, have attracted considerable attention as structurally simple and modifiable scaffolds for developing MAO-B inhibitors. Their α,β-unsaturated carbonyl framework acts as a Michael acceptor, facilitating interactions with the flavin adenine dinucleotide (FAD) cofactor within MAO-B.[12,13] Owing to their synthetic accessibility, tunable physicochemical properties, and favorable brain permeability, chalcones are considered promising leads for multifunctional neuroprotective agents.

MAO-B inhibition remains a central therapeutic strategy in PD management, especially for the early-stage patients with motor fluctuations.[14,15] Selegiline, an early-generation irreversible selective MAO-B inhibitor, is clinically effective but produces amphetamine-like metabolites that can elicit insomnia, irritability, and hypertension.[16] Rasagiline,

developed as a second-generation analogue, avoids such metabolites and displays improved tolerability, though its neuroprotective and disease-modifying potential remains debated.[17] Safinamide, a more recent addition, exhibits reversible MAO-B inhibition alongside modulation of glutamate release, thus addressing both motor symptoms and excitotoxic neuronal injury.[18] Notably, its fluorobenzyloxy structural motif has inspired new MAO-B inhibitors with enhanced pharmacological profiles, where fluorine substitution improves lipophilicity, blood–brain barrier permeability, and metabolic stability.[19–22]

Building upon this rationale, chalcone-based MAO-B inhibitors have been widely explored to enhance potency, selectivity, and CNS penetration.[23–25] Early work by Chimenti *et al.* (2009) introduced 2-hydroxy and 4-benzyloxy-substituted chalcones as potent, reversible MAO-B inhibitors exhibiting antioxidant and neuroprotective activity.[12,24] Subsequent modifications aimed to improve blood–brain barrier permeability and reduce MAO-A affinity, thereby minimizing off-target effects.[25] Benzyloxy substitution, particularly at the *para* position of the B-ring, has proven especially effective in enhancing hydrophobic contacts within the MAO-B active site, improving binding affinity and
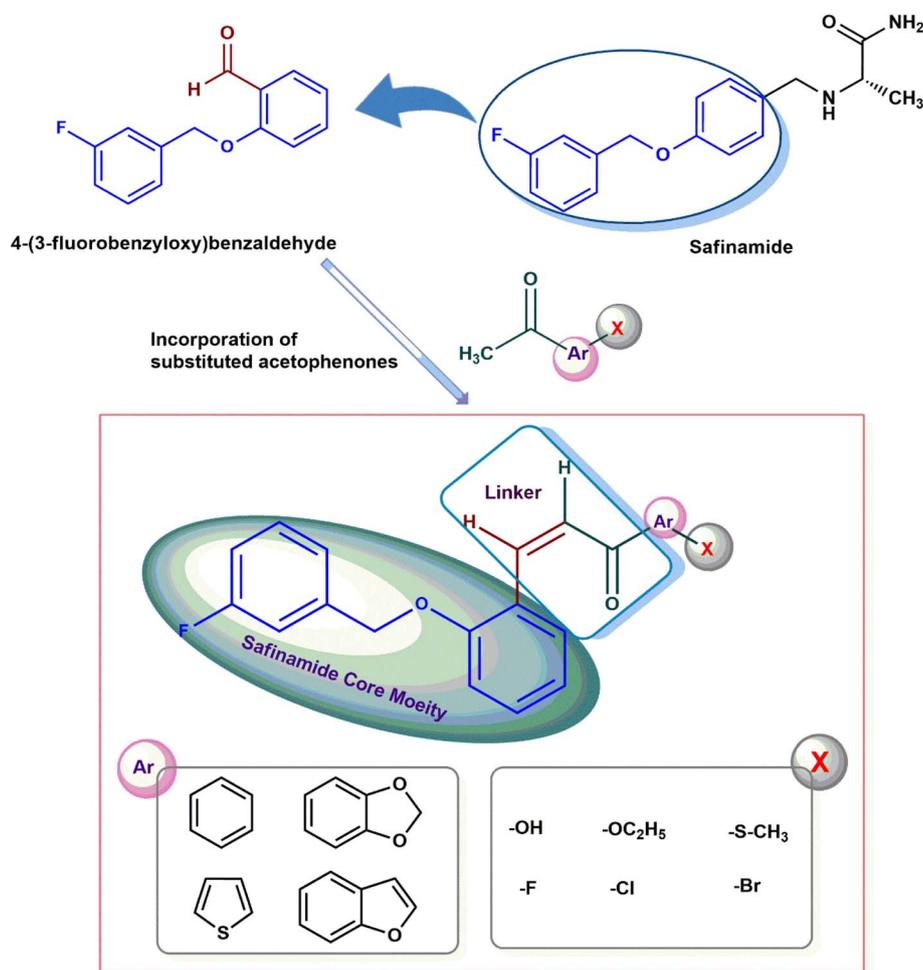

Fig. 1 Design strategy of fluorobenzyloxy derivatives.

isoform selectivity.[26,27] Furthermore, halogen substituents such as fluorine, chlorine, and bromine contribute to favorable pharmacokinetic and binding properties *via* halogen bonding and increased lipophilicity.[28,29]

Structure–activity relationship (SAR) investigations have revealed that the position and nature of benzyloxy and halogen substituents critically influence MAO-B inhibition.[11,15,30–32]

Benzyloxy derivatives with *para* substitution typically demonstrate superior inhibition compared to *ortho*-substituted analogues, likely due to optimal orientation within hydrophobic pockets and reduced steric hindrance.[27,29,33] The –CH$_2$O– linker introduces conformational flexibility, enabling better accommodation of the FAD-binding cavity. Despite extensive exploration of benzyloxy and halogenated chalcones, fluorinated benzyloxy analogues remain largely underexplored, especially those combining safinamide-like fluorobenzyl motifs with chalcone frameworks.[34]

In this context, we designed and synthesized a series of fluorinated benzyloxy chalcones integrating the pharmacophoric 4-(3-fluorobenzyloxy)phenyl unit as found in safinamide with halogenated acetophenone derivatives (Fig. 1). The synthesized compounds were evaluated for MAO-B inhibition, reversibility, kinetics, PAMPA-based permeability, and antioxidant studies. Molecular docking and molecular dynamics simulations were employed to elucidate the binding interactions and conformational stability within the MAO-B active site. This study builds upon prior findings where *para*-benzyloxy chalcones, (*E*)-3-(4-(benzyloxy)phenyl)-1-(thiophen-2-yl)prop-2-en-1-one (**B10**) and (*E*)-3-(4-(benzyloxy)phenyl)-1-(4-ethoxyphenyl)prop-2-en-1-one (**B15**) exhibited submicromolar MAO-B inhibition and good selectivity, yet lacked fluorine-mediated lipophilicity enhancement.[26] By incorporating a fluorinated benzyloxy moiety, this work aims to expand the chemical space of reversible and selective MAO-B inhibitors with improved brain permeability and potential neuroprotective activity. These hybrid fluorobenzyloxy chalcones therefore represent a structurally unexplored and pharmacologically promising class of MAO-B inhibitors for PD therapy.

2 Materials and methods

2.1. Synthesis

Equimolar quantities of substituted acetophenone (0.01 mol) and fluorobenzyloxy benzaldehyde (0.01 mol) were dissolved in 25 mL of absolute ethanol in a 100 mL round-bottom flask equipped with a magnetic stirrer. To this solution, 7.5 mL of 40% aqueous potassium hydroxide was added dropwise with constant stirring at room temperature (25–28 °C). The reaction mixture was stirred for 20–24 h, and progress was monitored periodically by thin-layer chromatography (TLC) on pre-coated silica gel 60 F254 plates (Merck) using a hexane : ethyl acetate (9 : 1) solvent system. Upon completion, the reaction mixture was poured onto crushed ice with continuous stirring to obtain a yellow precipitate. The solid was filtered under vacuum, washed with cold distilled water until neutral, and air-dried. The crude product was recrystallized from methanol or ethanol to afford the pure chalcone derivatives (Scheme 1).

All chemicals and solvents were procured from Sigma-Aldrich or Merck. Melting points of synthesised compounds were determined using a digital melting point apparatus (Electronics India) and were uncorrected. Reaction monitoring was performed under UV light (254 nm).

2.2. Enzyme assays

The enzyme activities of human MAO-A and MAO-B (recombinant, Sigma-Aldrich, St. Louis, MO, USA) were evaluated using 0.06 mM kynuramine and 0.3 mM benzylamine, respectively.[35–38] The substrate concentrations were about $2 \times K_m$ values, respectively. Absorbance of each reaction was measured for 45 min at room temperature in a cuvette containing 500 μL reaction mixture using the continuous method at 250 nm or 316 nm, respectively, as described previously. The reactions were initiated by adding each substrate to the reaction mixtures.

2.3. Inhibition study of MAO-A and MAO-B by the compounds and kinetics

In the primary screening, thirteen compounds were evaluated for their inhibition of MAO-A or MAO-B at 40 μM concentration. The half-inhibitory concentration (IC$_{50}$) of the compounds were calculated by using GraphPad Prism software 5.[35] The upper limit IC$_{50}$ value was 40 μM and the values higher than that were shown as >40 μM. The selectivity index (SI) was represented by calculating as IC$_{50}$ of MAO-A/IC$_{50}$ of MAO-B. The inhibitions of compounds were compared with reference inhibitors; toloxatone and clorgyline (reversible and irreversible inhibitor, respectively) for MAO-A, safinamide and pargyline (reversible and irreversible inhibitor, respectively) for MAO-B inhibitors.[35–38] In the kinetic study, a Lineweaver–Burk (LB) plot was generated using five substrate concentrations (0.0375 to 0.6 mM) around the K_m value (0.35 mM) of benzylamine for MAO-B. For the inhibition kinetics, lead compounds (*E*)-3-(2-((3-fluorobenzyl)oxy)phenyl)-1-(thiophen-2-yl)prop-2-en-1-one (**FBZ6**) and (*E*)-1-(4-bromophenyl)-3-(2-((3-fluorobenzyl)oxy)phenyl)prop-2-en-1-one (**FBZ13**) were used at three concentrations, approximately 0.5-, 1.5-, and 2.0-times their IC$_{50}$ values, and the inhibition constant (K_i) was determined using the secondary plot of their slopes in the LB plots.

2.4. Reversibility studies

The reversibility of the lead compounds **FBZ6** and **FBZ13** for MAO-B were evaluated using dialyzer tube (D-Tube Dialyzer Maxi, MWCO 6–8 kDa, Sigma-Aldrich, St. Louis, MO, USA) for dialysis method. Their reversibility were analyzed by the values of undialyzed (A_U) and dialyzed (A_D) activities, measuring approximately 2.0-times their IC$_{50}$ values after pre-incubation for 30 min each.[35–38] Reversibility patterns of lead compounds were determined by comparing the A_U and A_D to those of the references.

2.5. Blood–brain barrier (BBB) permeability study

In early drug research, the Parallel Artificial Membrane Permeation Assay (PAMPA) is employed to estimate

Scheme 1 Synthesis of fluorobenzyloxy chalcones (**FBZ1–FBZ13**).

a medication's passive transcellular permeability across the blood–brain barrier (BBB). The PAMPA setup involved constructing a sandwich-like structure using a 96-well Microtiter plate and a 96-well Millipore filter plate (specifically, an IPVH filter, 125 μm thick with 0.45 μm pores). Following this, 0.1 mL of *n*-dodecane was added to the plates. Drug preparation involved making 10 mM stock solutions in DMSO, which were stored at 0 °C until use. Before introduction to the assay plate, these stock solutions were further diluted in a pH 7.4 buffer. This critical dilution step maintained the DMSO content at a maximum of 1% (v/v) and resulted in final drug sample concentrations of 0.01, 0.1, 0.5, and 1 mM. For the assay, 200 μL of pH 7.4 buffer filled the acceptor wells, while 270 μL of the prepared drug solutions were aliquoted into the donor wells. The "sandwich" arrangement was completed by carefully aligning and placing the acceptor filter plate directly over the donor plate. This configuration comprises an aqueous donor compartment (containing the analyte) at the bottom, an artificial lipid barrier in the middle, and an aqueous recipient compartment at the top. During the assay, the tested substance diffuses from the donor well, through the lipid membrane, and into the acceptor well. The structural integrity of this "sandwich" was confirmed to be maintained throughout the experiment. Finally, the concentrations of the drug in the donor, recipient, and reference wells were determined using UV spectroscopy, and the degree of penetration (permeability) was subsequently computed *via* an established equation.[26,39]

$$\text{Log } P_e = -\ln[1 - C_A/E_{\text{quilibrium}}]/A \times (1/V_D + 1/V_A) \times t$$

where, P_e is permeability (cm s^{-1}), C_A = receptor concentration, A = area of effective filtration (4.8 cm^2), V_D = donor volume (ml), V_A = acceptor volume (ml), t = time of incubation (s) and $E_{\text{quilibrium}} = (C_D \times V_D + C_A \times V_A)/(V_D + V_A)$.

2.6. *In vitro* antioxidant enzyme activity assays

The antioxidant activities of the lead compounds **FBZ6** and **FBZ13** were investigated by quantifying the enzymatic activities of superoxide dismutase (SOD),[40,41] glutathione assay (GSH),[42,43] glutathione peroxidase (GPX),[44,45] and catalase (CAT),[44,46] in SH-SY5Y human bone marrow neuroblastoma cell lines. The SI contains a comprehensive description of the experimental methods.

2.7. Molecular docking

The hMAO-B protein structure (PDB code: 2V5Z) was obtained from the RCSB database and processed with the Protein Preparation Wizard in Maestro. This involved adjusting bond orders, removing extraneous components, and fixing structural issues such as missing atoms, loops, and side chains.[47,48] Afterward, a grid was created using a co-crystallized ligand. The OPLS-2005 force field was applied throughout both the protein preparation and simulation processes. The 2D structures were then imported into Maestro's LigPrep module to convert them into 3D forms, where LigPrep added hydrogen atoms, generated stereoisomers, and optimized ligand geometry. The 'Epik' module calculated possible ionization states at pH 7 ± 0.0, with a single ligand conformation generated. The OPLS-2005 force field was used across the ligand preparation protocol.[49]

Preceding High-Throughput Virtual Screening (HTVS), the molecules in the library undergo screening applying Lipinski's rule of five for risk evaluation as well as *in silico* forecasting of bioavailability of molecules. In order to assess the ligand-targeted protein binding affinity, the desired protein is brought onto the Maestro environment for docking. The molecules were docked using three steps of docking: HTVS, Standard Precision (SP), and Extra Precision (XP).[49–51] The materials underwent a multiple step docking process based on Glide. Every database utilised during the research underwent identical docking and screening procedures.

2.8. Molecular dynamic (MD) simulation

For an assessment of the ligand–receptor binding mode and the stability of the complex, molecular dynamics simulation is carried out over a 200 ns period. The experiment was performed on a Linux system using the Schrodinger Desmond module. Employing an orthorhombic box shape as the boundary constraint, the protein–ligand complexes was solvated using SPC water model.[52] Na^+ and Cl^- salts being introduced to the system at a concentration of 0.15 M in order to neutralise it. Using Nose–Hoover thermal coupling at 300 K and Martyna–Tobias–Klein pressure coupling at 1.01 bar constant pressure, NPT ensembles were employed in MD simulations. To assess the domain correlations, an RMSD, RMSF, and protein ligand contact analysis was constructed during the 200 ns MD simulation.[53–56]

3 Results and discussion

3.1. Chemistry

The fluorobenzyloxy chalcones were synthesized by the overnight stirring of various substituted acetophenones and *para*/

ortho-substituted benzyloxy benzaldehyde *via* the Claisen–Schmidt reaction (Scheme 1).[57,58] Specifically, equimolar amounts (0.01 M) of the respective acetophenone and fluorobenzyloxy benzaldehyde were dissolved in 25 mL of ethanol. A 40% aqueous KOH solution (7.5 mL) was then added dropwise as the final reagent, and the resulting mixture was kept for stirring at room temperature for 20–24 hours. Reaction progress was monitored by thin-layer chromatography (TLC) using silica gel plates and a hexane : ethyl acetate (9 : 1) mobile phase. Upon completion of the synthesis, evaluation using thin-layer chromatography (TLC) displayed single spot. The synthesized compounds were obtained as solid materials with yellow, pale yellow, dark yellow, or pale/light brown coloration. The isolated yields ranged from 61 to 89%. The crude product was then purified by recrystallization in ethanol (or alternative solvent), affording the final chalcone derivatives as pale-yellow crystalline solids and fine powders followed by flash chromatography. The compounds exhibited melting points in the range of 90–130 °C. They were moderately soluble in ethanol and methanol, freely soluble in chloroform and DMSO. 4-Chloro and 4-fluoro, consistently yielded higher (up to 89%) than their *ortho*-substituted counterparts, which produced as little as 61%. This trend is likely due to reduced steric hindrance and enhanced resonance stabilization in *para*-substituted systems, favoring efficient enolate formation and smoother condensation. Conversely, electron-donating groups like methoxy and hydroxy, despite stabilizing the aromatic ring, occasionally resulted in lower yields, possibly due to increased polarity impacting solubility and recrystallization. *Para*-substituted halogenated chalcones frequently crystallized as pale-yellow solids, indicating superior molecular packing and lattice organization. In contrast, *ortho*-substituted and heterocyclic analogues, particularly those with thiophene or benzodioxolone moieties, typically formed fine powders, likely due to steric hindrance and reduced symmetry disrupting regular crystal packing during recrystallization. All final derivatives were characterised using ¹H NMR, ¹³C NMR, and mass spectrometry. The ¹H NMR data revealed sharp doublet peaks for Hα and Hβ at δ 7.78 and within the multiplet region at δ 7.90–7.84 for **FBZ13**, and at δ 7.27 and within the multiplet region at δ 7.87–7.79 for **FBZ6**, confirming a *trans* (E)-configuration across the α,β-unsaturated carbon–carbon double bond. The methylene protons of the benzyloxy linkage appeared as singlets at δ 5.11 in both spectra. Aromatic protons were observed in the δ 7.00–7.87 range, reflecting contributions from substituted aryl and heteroaryl rings including the bromophenyl ring in **FBZ13** and the thiophene ring in **FBZ6**. In the ¹³C NMR spectra, the deshielded carbonyl carbons of the chalcone moiety appeared at δ 189.36 (**FBZ13**) and δ 182.04 (**FBZ6**). Signals near δ 160–164 were attributed to electron-deficient aromatic carbons bearing fluorine and oxygen substituents, while the benzylic carbon resonated at $\delta \sim 69.3$ in both compounds. The ESI-MS spectra confirmed the expected molecular formulas, showing $[M + H]^+$ peaks at m/z 411.3698 for **FBZ13** and m/z 338.3998 for **FBZ6** [SI].

3.2. Inhibition study of MAO-A and MAO-B by the compounds

Thirteen 4-(3-fluoro-benzyloxy) chalcone derivatives were evaluated for their inhibitory activities against MAO-A and MAO-B. All compounds showed higher MAO-B inhibition than MAO-A (Table 1). Compound **FBZ13** showed the most potent MAO-B inhibition with an IC_{50} value of 0.0053 μM, followed by **FBZ6**(IC_{50} = 0.023 μM) (Table 1). In addition, compounds **FBZ13** had high selectivity index (SI) of MAO-B over MAO-A (SI ≥ 7547.17) (Table 1). The IC_{50} value of **FBZ13** for MAO-B was 4.0 times lower than that of safinamide (a reference MAO-B inhibitor, IC_{50} = 0.021 μM), and lower than those of a chalcone-based oxime derivative **CHBO4** (IC_{50} = 0.031 μM),[59] a isopropyl chalcone **CA4** (IC_{50} = 0.032 μM),[49] benzyloxy-derived halogenated chalcone BB4 (IC_{50} = 0.062 μM),[27] and a benzimidazole chalcone **BCH2** (IC_{50} = 0.80 μM),[60] and similar to those of a oxygenated chalcone O23 (IC_{50} = 0.0021 μM),[61] and a multiconjugated dienone **MK6** (IC_{50} = 0.0028 μM).[62] In addition, the SI value of **FBZ13** was much higher than that of safinamide (>1904).

In comparison to these reported scaffolds, the fluorinated benzyloxy chalcones in this study exhibit a unique combination of low nanomolar MAO-B inhibition and high selectivity, particularly notable in **FBZ13**. While chalcones like O23 and MK6 have shown similar or slightly superior potency, their frameworks rely heavily on polyoxygenation or extended conjugation systems, which may affect metabolic stability or brain penetration. In contrast, **FBZ13** integrates a strategically positioned 3-fluorobenzyloxy moiety on the B-ring—a feature inspired by the safinamide pharmacophore—that has not been extensively explored in chalcone-based MAO-B inhibitors.

Additionally, compared to **BB4** and **CA4**, which also possess halogenated benzyloxy or isopropyl side chains, **FBZ13** demonstrates superior potency and selectivity. These differences may arise from enhanced halogen bonding and favorable hydrophobic interactions within the MAO-B active site, as predicted by docking. The 3-fluoro substituent likely enhances electronic and lipophilic interactions without introducing excessive steric hindrance, a feature not exploited in previous scaffolds.

3.3. Enzyme kinetics

Enzyme and inhibition kinetics of MAO-B by **FBZ6** and **FBZ13** were analyzed at five concentrations of benzylamine as a substrate and at three inhibitor concentrations. In LB plots, four lines of **FBZ6** or **FBZ13** met at a point on y-axis and appeared to be competitive MAO-B inhibitors (Fig. 2A and C). Their secondary plots showed that the K_i values were 0.015 ± 0.003 and 0.0021 ± 0.0013 μM, respectively (Fig. 2B and D). These results suggest that **FBZ6** and **FBZ13** are potent competitive MAO-B inhibitors.

3.4. Reversibility studies

In reversibility study, concentrations of **FBZ6** and **FBZ13** used were approximately 2.0-times of their IC_{50} values (0.040 and 0.010 μM for MAO-B, respectively). Residual activities before and after recovery were represented by A_U and A_D. Compounds **FBZ6** and **FBZ13** were recovered from 33.98% to 83.64% and from 30.34% to 88.18%, respectively (Fig. 3). The recovery values of **FBZ6** and **FBZ13** were similar to those of safinamide, a reversible MAO-B inhibitor, (ranging from 29.29% to 82.50%), whereas they differed from those of pargyline (ranging from 32.03% to 35.59%). These results indicated that **FBZ6** and **FBZ13** were reversible MAO-B inhibitors, as likely safinamide.

3.5. Structure–activity relationships (SAR)

Compound (E)-1-(4-bromophenyl)-3-(2-((3-fluorobenzyl)oxy) phenyl)prop-2-en-1-one (**FBZ13**), bearing a 4-Br substituent on the phenyl ring, exhibited 4.34- to 91.13-fold higher MAO-B inhibition than other derivatives. When compared according to the position of the substituent on the phenyl ring, **FBZ13** showed superior activity in the order: 4-Br (**FBZ13**) > 4-OH (**FBZ2**) > 2-F (**FBZ5**) > 2-Cl (**FBZ9**) > 4-Cl (**FBZ10**) > –H (**FBZ1**) > 4-F (**FBZ12**) > 4-SCH₃ (**FBZ5**). These results indicate that 4-Br and 2-F substituents on the phenyl ring are most influential in enhancing MAO-B inhibition. A focused comparison of 4-position substituents further confirmed the trend: –Br (**FBZ13**) > –OH (**FBZ2**) > –Cl (**FBZ10**) > –H (**FBZ1**) > –F (**FBZ12**) > –SCH₃ (**FBZ5**). Additionally, the thiophene-substituted compound **FBZ6** demonstrated high MAO-B inhibition. Substitution of bromine at the 4-position in **FBZ7** led to a significant drop in activity, suggesting that both the nature and orientation of the substituent are critical. Among halogenated derivatives, ortho-substitution (e.g., **FBZ9** and **FBZ11**) generally yielded better MAO-B inhibition than para-substitution (e.g., **FBZ10** and **FBZ12**), highlighting the importance of steric orientation and proximity to the carbonyl group in influencing molecular conformation and enzyme interaction (Fig. 4).

Table 1 Inhibitions of MAO-A and MAO-B by the FBZ series[a]

| Compounds | IC₅₀ (μM) | | SI[b] |
	MAO-A	MAO-B	
FBZ1	>40	0.091 ± 0.008	>439.56
FBZ2	3.178 ± 0.011	0.065 ± 0.002	48.89
FBZ3	>40	0.476 ± 0.099	>84.03
FBZ4	3.891 ± 0.023	0.483 ± 0.056	8.06
FBZ5	>40	0.187 ± 0.003	>213.90
FBZ6	28.921 ± 1.743	**0.023 ± 0.001**	1257.44
FBZ7	>40	0.241 ± 0.065	>1659.75
FBZ8	25.930 ± 0.728	0.463 ± 0.007	56.00
FBZ9	>40	0.079 ± 0.008	>506.33
FBZ10	>40	0.082 ± 0.012	>487.80
FBZ11	16.510 ± 1.634	0.077 ± 0.009	214.42
FBZ12	>40	0.103 ± 0.008	>388.35
FBZ13	>40	**0.0053 ± 0.0020**	>7547.17
Toloxatone	1.245 ± 0.233	>40	>32.13
Clorgyline	0.013 ± 0.008	1.853 ± 0.112	142.54
Safinamide	>40	0.021 ± 0.001	>1904
Pargyline	2.403 ± 0.358	0.14 ± 0.01	17.16

[a] Results are the means ± standard errors of duplicate or triplicate experiments. [b] Selectivity index (SI) values are expressed for IC_{50} of MAO-B versus IC_{50} of MAO-A.
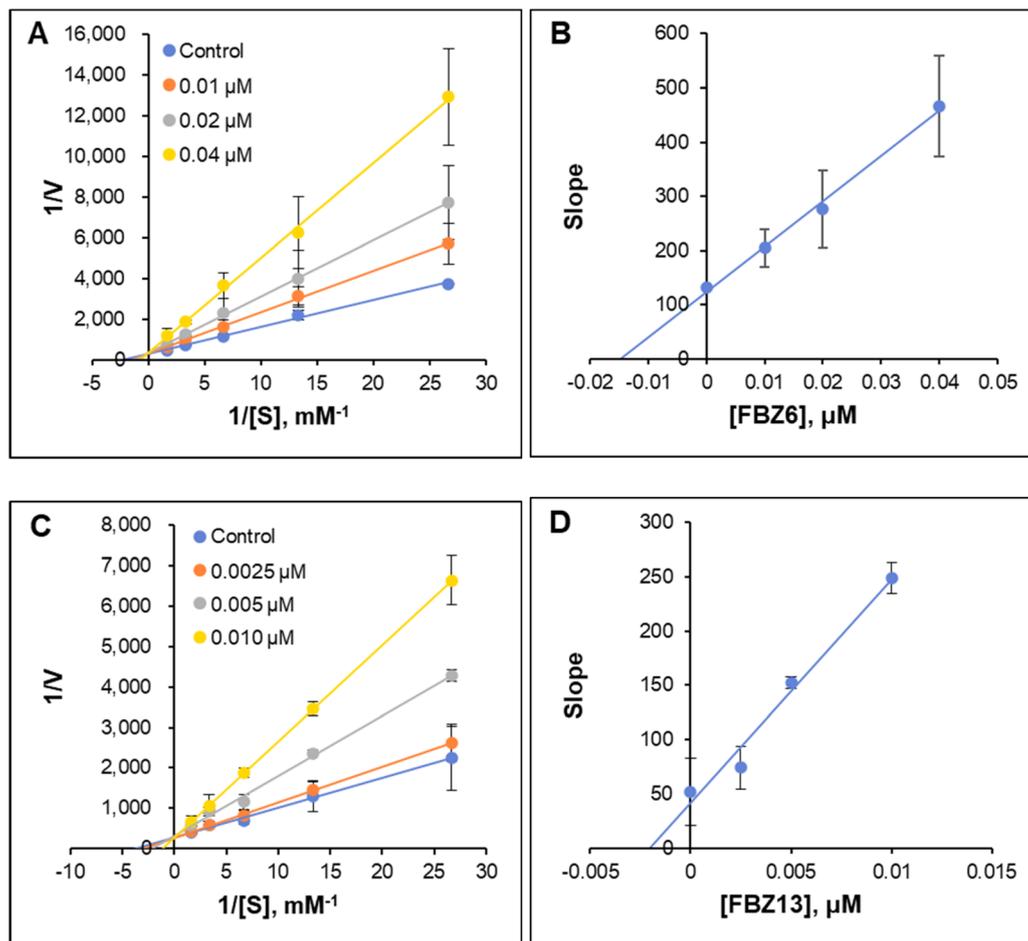
Fig. 2 Lineweaver−Burk (LB) plots for MAO-B inhibition by **FBZ6** and **FBZ13** (A and C), and their secondary plots (B and D) of the slopes *versus* inhibitor concentrations. The experiments were analyzed using five concentrations of substrate and three concentrations of inhibitor.
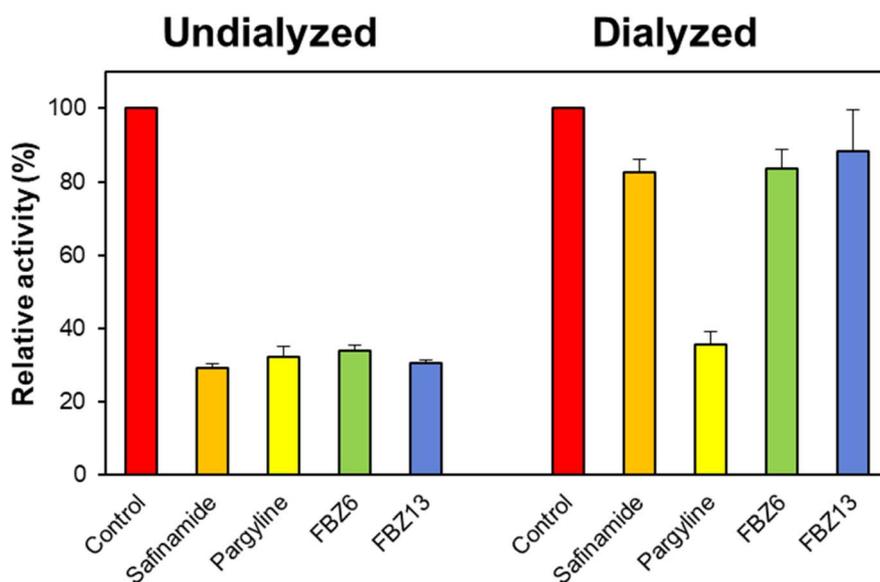

Fig. 3 Recovery of MAO-B inhibition by **FBZ6** and **FBZ13** using dialysis experiments. The concentrations of **FBZ6** and **FBZ13** used were ~2.0-times of their IC_{50} values (0.040 and 0.010 μM). After a 30 min pre-incubation, the mixtures were dialyzed for 6 h with two buffer changes.

Electron-withdrawing groups such as –Br and –F at the *para* and *ortho* positions enhanced MAO-B inhibition, likely due to increased lipophilicity and favorable interactions within the hydrophobic active site. In contrast, electron-donating groups such as –SCH$_3$ and –OH exhibited moderate inhibition, possibly due to a reduced binding affinity. These findings align with recent reports on chalcone-based MAO-B inhibitors. 1-(4-Bromophenyl)-3-(4-fluorophenyl) prop-2-en-1-one oxime (**CHBO4**), a chalcone-based oxime derivative, reported an IC$_{50}$ of 0.031 μM,[59] whereas **FBZ13** exhibited a 1.5-fold lower IC$_{50}$, indicating enhanced potency. (*E*)-1-(4-Hydroxyphenyl)-3-(4-isopropylphenyl) prop-2-en-1-one (**CA4**), an isopropyl chalcone, showed an IC$_{50}$ of 0.032 μM,[49] and the IC$_{50}$ of **FBZ13** was approximately 1.5-fold lower. 4 (2*Z*)-3-[4-(Benzyloxy)phenyl]-1-(4-bromophenyl)prop-2-en-1-one (**BB4**), a benzyloxy-derived halogenated chalcone, demonstrated an IC$_{50}$ of 0.062 μM,[27] nearly 3-fold higher than **FBZ13**. (*E*)-1-(1*H*-Benzo[*d*]imidazol-2-yl)-3-(2-chlorophenyl)prop-2-en-1-one (**BCH2**), a benzimidazole chalcone, exhibited an IC$_{50}$ of 0.80 μM,[60] making **FBZ13** approximately 38-fold more potent. Although oxygenated chalcone, (2*E*)-1-(2,3-dihydro-1,4-benzodioxin-6-yl)-3-(4-fluorophenyl)prop-2-en-1-one (**O23**) (IC$_{50}$ = 0.0021 μM)[61] and multiconjugated dienone, (2*E*,4*E*)-1-(4-bromophenyl)-5-phenylpenta-2,4-dien-1-one (**MK6**) (IC$_{50}$ = 0.0028 μM)[62] showed slightly superior MAO-B potency than **FBZ13**. Compounds (2*E*)-3-(4-chlorophenyl)-1-[4-(methylsulfanyl)phenyl]prop-2-en-1-one (**TM8**), a thiomethyl chalcone derivative (MAO-B IC$_{50}$ = 0.010 μM),[63] (*E*)-3-(2-chlorophenyl)-1-(2,4-dimethoxyphenyl)prop-2-en-1-one (**DM2**), a dimethoxy-halogenated chalcone (MAO-B IC$_{50}$ = 0.067 μM),[64] (*E*)-3-phenyl-1-(4-(piperazin-1-yl)phenyl)prop-2-en-1-one (**PC1**), piperazine-based chalcone, (MAO-B IC$_{50}$ = 7.62 μM),[65] and (*E*)-3-(4-fluoro-3-(trifluoromethyl)phenyl)-1-(4-(4-methylpiperazin-1-yl)phenyl)prop-2-en-1-one (**2k**), a 3-trifluoromethyl-4-fluorinated derivative, (MAO-B IC$_{50}$ = 0.71 μM),[66] showed less potency when compared with **FBZ13**. Compared to the most of these reported chalcone analogs, **FBZ13** demonstrates significantly enhanced potency and selectivity, reinforcing its therapeutic potential.

The IC$_{50}$ value of **FBZ13** was also 4.0 times lower than that of safinamide (IC$_{50}$ = 0.021 μM), and its selectivity index (SI > 1904) was significantly higher, indicating superior MAO-B selectivity. In comparison to these reported scaffolds, the fluorinated benzyloxy chalcones in this study exhibit a unique combination of low nanomolar MAO-B inhibition and high selectivity, particularly notable in **FBZ13**. **FBZ13** integrates a strategically positioned 3-fluorobenzyloxy moiety on the B-ring feature inspired by the safinamide pharmacophore that has not been extensively explored in chalcone-based MAO-B inhibitors. This structural innovation contributes to both potency and selectivity, reinforcing the novelty and therapeutic relevance of our scaffold.

3.6. Parallel artificial membrane permeability assay (PAMPA) for blood–brain barrier (BBB) permeation study

PAMPA manifested that the compounds **FBZ6** and **FBZ13** showcased a substantial level of permeability and CNS bioavailability. Remarkable Pe values larger than 4.0×10^{-6} cm
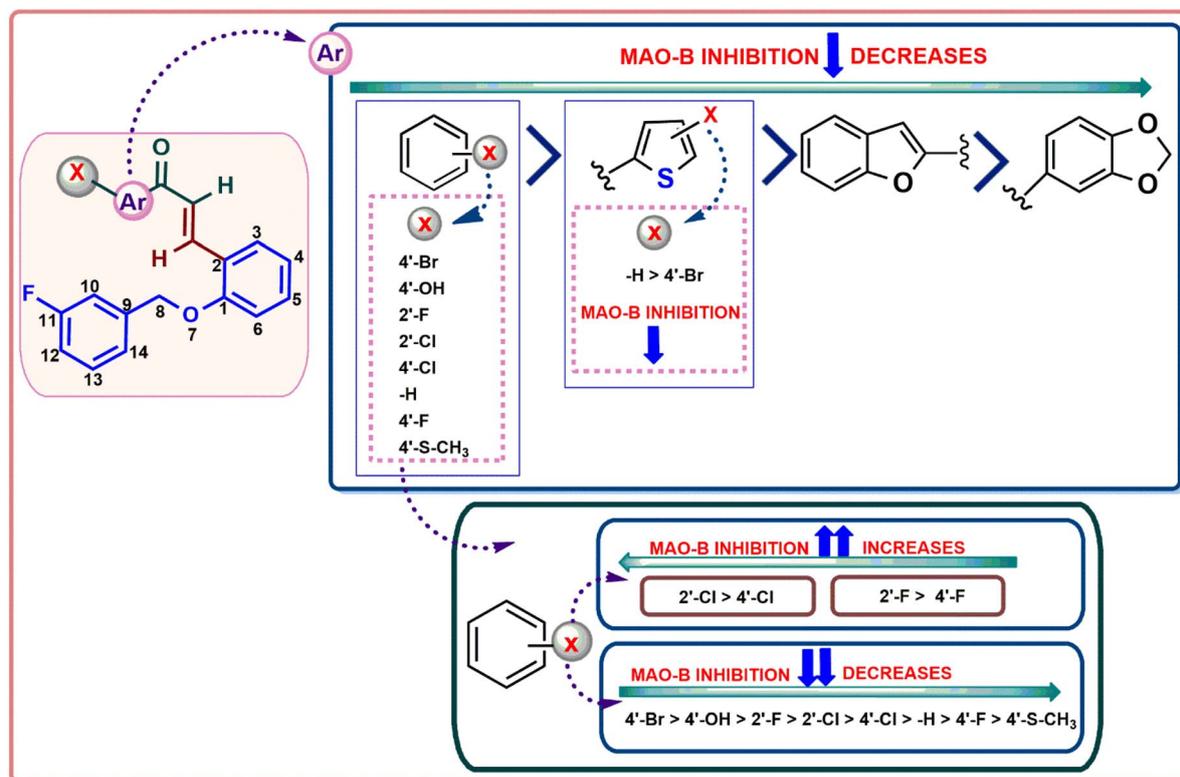

Fig. 4 SAR of fluorobenzyloxy derivatives.

Table 2 Blood–Brain Barrier assay of key compounds by PAMPA method

Compounds	Experimental Pe[a,b] ($\times 10^{-6}$ cm s^{-1})	Prediction
FBZ6	7.70 ± 0.12	CNS+
FBZ13	9.78 ± 0.09	CNS+
Selegiline	5.69 ± 0.04	CNS+

[a] Results are the means $\pm$ standard errors of duplicate or triplicate experiments. [b] Pe (10^{-6} cm s^{-1}) > 4.00: CNS+ (high permeation); Pe (10^{-6} cm s^{-1}) < 2.00: CNS− (low permeation); Pe (10^{-6} cm s^{-1}) from 2.00 to 4.00: CNS$\pm$ (BBB permeation uncertain).

s^{-1} were found in **FBZ6** and **FBZ13**, suggesting higher BBB penetration rates of 7.70×10^{-6} cm s^{-1} and 9.78×10^{-6} cm s^{-1}, respectively (Table 2).

Neurological drug administration necessitates brain penetration. PAMPA-BBB is used in the current study to measure each derivative's brain permeability. The penetration depth may be computed employing the formula and the compound's effective permeability (log P). Molecules identified as potentially permeating (CNS+) had Pe values more than 4.0×10^{-6} cm s^{-1}, whereas molecules evaluated as presumably non-BBB penetrating (CNS−) had Pe values less than 2.0×10^{-6} cm s^{-1}.

Selegiline, a clinically approved irreversible MAO-B inhibitor, was used as the reference standard in the current study and exhibited a Pe value of $5.69 \pm 0.04 \times 10^{-6}$ cm s^{-1}. In comparison, both **FBZ6** ($7.70 \pm 0.12 \times 10^{-6}$ cm s^{-1}) and **FBZ13** ($9.78 \pm 0.09 \times 10^{-6}$ cm s^{-1}) demonstrated significantly higher permeability values. This indicates superior BBB penetration potential for the synthesized derivatives, which may translate to improved CNS exposure. Since MAO-B is predominantly expressed in brain regions like the basal ganglia, effective BBB crossing is crucial for therapeutic efficacy. Enhanced permeability also suggests a better pharmacokinetic profile, possibly leading to faster onset and more sustained action. Thus, **FBZ6** and **FBZ13** may offer pharmacological advantages over selegiline in terms of CNS bioavailability and MAO-B targeting in Parkinson's disease.

3.7. *In vitro* antioxidant enzyme activity assays

Cellular anti-oxidant study was performed by measuring the relating enzymes such as SOD, CAT, GSH, and GPx in LPS-induced model of human neuroblastoma SH-SY5Y cells. While untreated sample showed high expression of enzymatic activities, LPS treated sample at 1 μg mL^{-1} inhibited the expression of all the anti-oxidant enzymes. However, **FBZ6** or **FBZ13** at 10 μM concentration showed significant recovery of enzyme activities by suppressing the inflammatory activity caused by LPS.

3.7.1. SOD assay. The SOD assay results revealed that both **FBZ6** and **FBZ13** showed a dose-dependent protective effect against LPS-induced oxidative stress. In untreated cells, the SOD levels were high (56.15 ng mL^{-1}), representing normal antioxidant activity. Treatment with LPS (1 μg) alone drastically reduced SOD levels to 10.50 ng mL^{-1}, indicating significant oxidative stress. Treatment with **FBZ6** led to a gradual restoration of SOD levels with increasing concentrations, 10.32 ng mL^{-1} at 1.0 μM to 42.64 ng mL^{-1} at 10 μM (Fig. 5A). Similarly, **FBZ13** demonstrated the restoration of SOD levels, but with a stronger antioxidant effect, 13.62 ng mL^{-1} at 1 μM to 44.07 ng mL^{-1} (Fig. 5B). These results indicate that both compounds can mitigate LPS-induced oxidative damage.

3.7.2. Glutathione assay (GSH). The results of the GSH assay reveal the protective effects of **FBZ13** and **FBZ6** against oxidative stress induced by lipopolysaccharide (LPS, 1 μg). The untreated control group exhibited the highest GSH levels (16.68 ng mL^{-1}), representing the baseline antioxidant capacity. However, LPS treatment alone significantly decreased GSH levels (2.44 ng mL^{-1}), underscoring the oxidative stress and decrease in intracellular antioxidant reserves brought on by LPS exposure. Following **FBZ6** treatment, GSH levels gradually increased with increasing doses, rising from 3.11 ng mL^{-1} at 1.0 μM to 12.36 ng mL^{-1} at 10 μM (Fig. 6A). With a higher antioxidant activity, **FBZ13** also showed that GSH levels were restored, rising from 3.66 ng mL^{-1} at 1 μM to 14.03 ng mL^{-1} (Fig. 6B). According to these findings, these compounds can attenuate the oxidative damage brought on by LPS.

Importantly, the restoration of SOD activity highlights the potential neuroprotective properties of **FBZ6** and **FBZ13**. Oxidative stress, marked by the depletion of endogenous antioxidant enzymes like SOD, plays a central role in the degeneration of dopaminergic neurons in PD. By restoring SOD levels in LPS-challenged cells, these compounds not only reduce oxidative burden but may also help maintain neuronal integrity. The higher SOD recovery seen with **FBZ13** suggests its stronger antioxidant capability, which could correlate with more pronounced neuroprotective effects *in vivo*. This antioxidant mechanism complements MAO-B inhibition, providing a dual mode of action enzyme modulation and oxidative damage mitigation relevant for disease modification in PD.

3.7.3. Glutathione peroxidase assay (GPx). The glutathione peroxidase (GPx) assay results demonstrated a significant protective effect of both **FBZ6** and **FBZ13** compounds against LPS-induced oxidative stress in a dose-dependent manner. The untreated control group exhibited baseline GPx levels of 326.46 ng mL^{-1}, while LPS treatment (1 μg) markedly reduced GPx concentration to 62.40 ng mL^{-1}, indicating severe oxidative stress. Following **FBZ6** treatment, GPx levels progressively elevated with escalating doses, rising from 77.69 ng mL^{-1} at 1.0 μM to 225.42 ng mL^{-1} at 10 μM (Fig. 7A). With a higher antioxidant activity, **FBZ13** also showed that GPx levels were restored, rising from 77.32 ng mL^{-1} at 1 μM to 298.04 ng mL^{-1} (Fig. 7B). These findings imply that these compounds can diminish the oxidative damage brought on by LPS.

The restoration of GPx levels following treatment with **FBZ6** and **FBZ13** suggests that these compounds can reinforce endogenous antioxidant defences in neural cells. GPx is a critical enzyme that detoxifies hydrogen peroxide and lipid peroxides, both of which are implicated in oxidative neuronal injury in PD. The dose-dependent increase in GPx, particularly with **FBZ13**, underscores its ability to mitigate reactive oxygen species and maintain redox balance. This mechanism, alongside MAO-B inhibition, supports a multifaceted neuroprotective
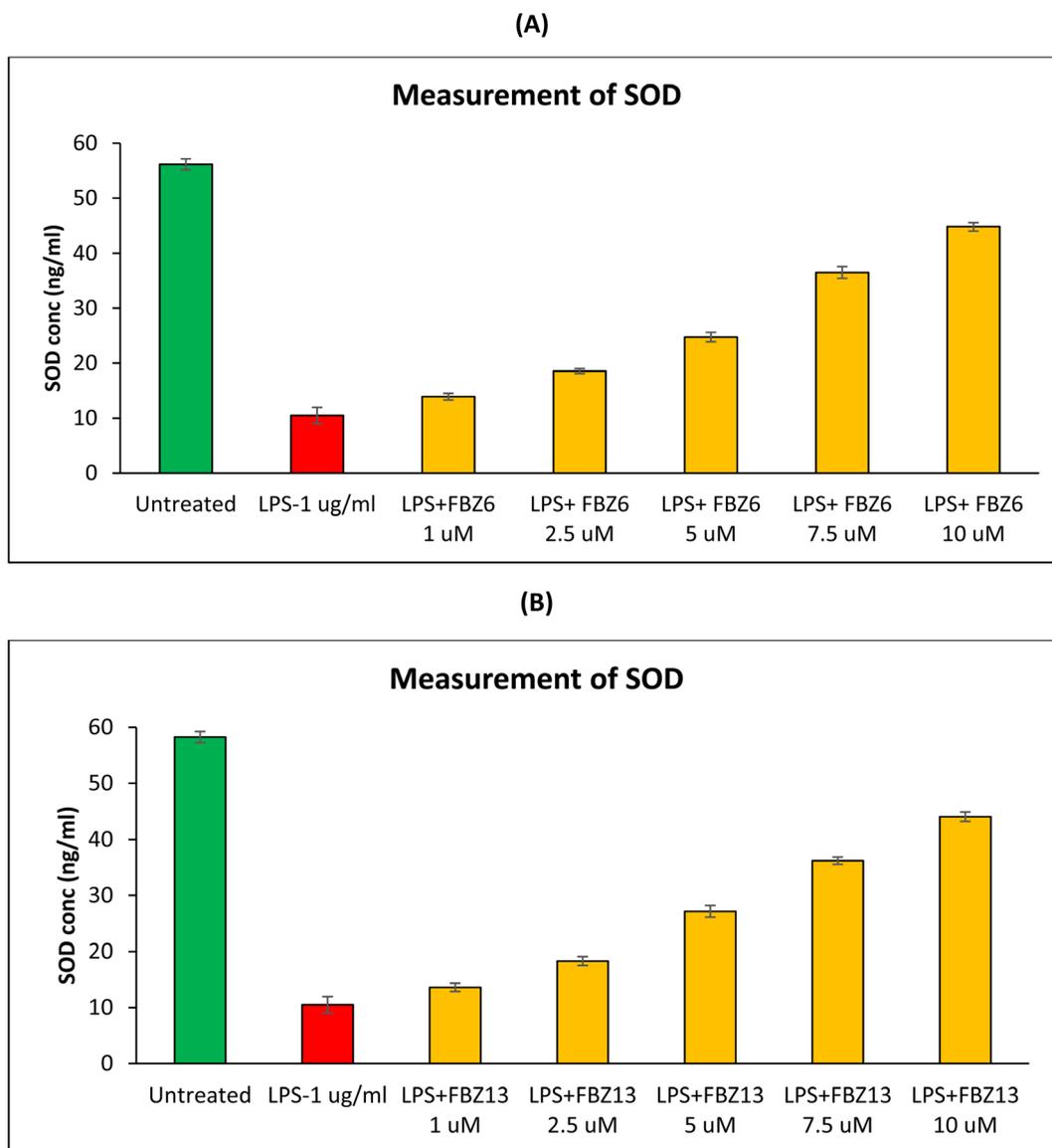
© 2025 The Author(s). Published by the Royal Society of Chemistry

Fig. 5 SOD levels observed in untreated, LPS alone, different concentrations of **FBZ6** (A) and **FBZ13** (B) treatment against the LPS induced SH-SY5Y cells after the incubation period of 24 h. Each assay was performed in duplicate.

profile that may help slow neurodegeneration and enhance neuronal survival in PD models.

3.7.4. Catalase assay (CAT). Both **FBZ6** and **FBZ13** compounds showed significant protective effects against LPS-induced oxidative stress, with a clear concentration-dependent response, according to the catalase (CAT) activity assay. LPS treatment (1 μg) significantly decreased CAT activity to 0.76 ng mL^{-1}, indicating severe oxidative stress and poor antioxidant defense, while untreated control conditions maintained CAT levels at 7.8 ng mL^{-1}. GPx levels upgraded with ascending doses following **FBZ6** treatment, from 1.02 ng mL^{-1} at 1.0 μM to 4.35 ng mL^{-1} at 10 μM (Fig. 8A). **FBZ13** also demonstrated that GPx levels were recovered with enhanced antioxidant activity, elevating from 0.82 ng mL^{-1} at 1 μM to 5.79 ng mL^{-1} (Fig. 8B). These results suggest that these compounds can alleviate oxidative damage triggered by LPS.

Catalase is vital for decomposing hydrogen peroxide, a reactive oxygen species (ROS) that contributes to oxidative damage in neural tissue. **FBZ6** and **FBZ13** demonstrated a concentration-dependent restoration of CAT activity, highlighting their potential to bolster the body's natural antioxidant defences, which is crucial in Parkinson's disease pathology. By enhancing catalase activity, these compounds may reduce oxidative stress-induced neuronal injury and inflammation, thus complementing their MAO-B inhibitory effects to provide neuroprotection and support CNS health.

3.8. Molecular docking

Based on the enzyme assay results, **FBZ13** and **FBZ6** demonstrated the highest efficacy and selectivity toward human MAO-B. To further explore their binding patterns and evaluate the influence of structural modifications on their inhibitory activity
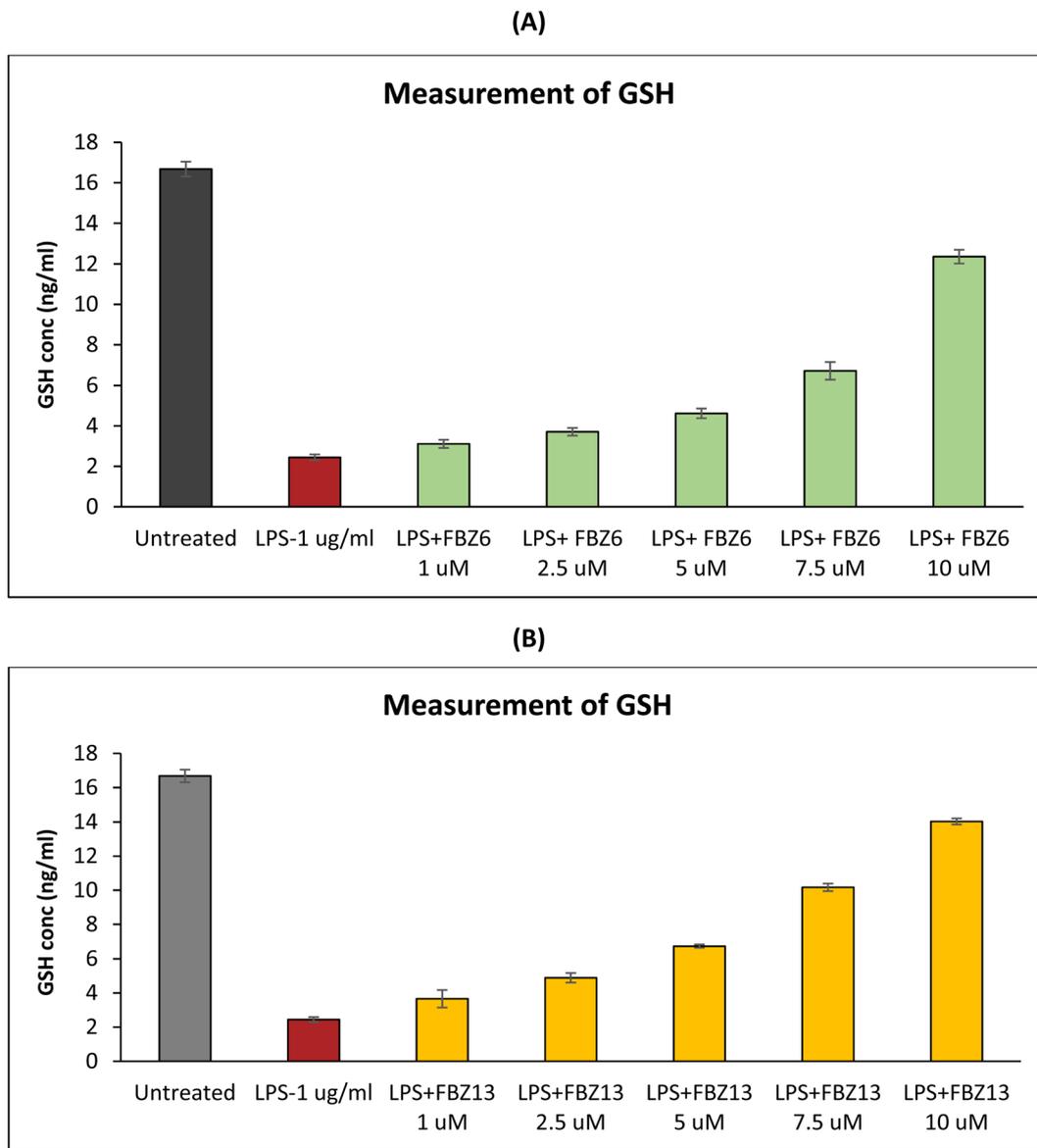
(A)

(B)

Fig. 6 GSH levels observed in untreated, LPS alone, different concentrations of **FBZ6** (A) and **FBZ13** (B) treatment against the LPS induced SH-SY5Y cells after the incubation period of 24 h. Each assay was performed in duplicate.

against MAO-B, docking studies were performed using PDB ID: 2V5Z. Both compounds exhibited notable docking scores, reinforcing their selectivity for MAO-B and aligning with the enzyme activity findings (Table 3). Among the two, **FBZ13** achieved the highest docking score of -11.302 kcal mol^{-1}. **FBZ6** followed closely with a docking score of -11.284 kcal mol^{-1}, while the reference drug safinamide recorded a docking score of -12.671 kcal mol^{-1}. Fig. 9 and 10 illustrate the two-dimensional and three-dimensional interactions of the lead compounds with MAO-B, respectively, with detailed binding interactions of **FBZ13** and **FBZ6**.

The interaction analysis of **FBZ6** and **FBZ13** with MAO-B reveals significant binding patterns contributing to their inhibitory activity. **FBZ6** forms strong hydrophobic interactions with residues such as LEU 328, TYR 326, PHE 343, and ILE 198,

stabilized further by interactions with TYR 188 and LEU 171. A hydrogen bond between the fluorine atom of **FBZ6** and the hydroxyl group of TYR 326 enhances its binding, while polar interactions with residues SER 59 and LYS 296 contribute to its specificity. Additionally, **FBZ6** exhibited π–π stacking interactions between its aromatic ring and the side chains of TYR 326 and PHE 343, which play a critical role in stabilizing the ligand within the hydrophobic pocket of MAO-B. In contrast, **FBZ13** exhibits robust hydrophobic interactions with residues including LEU 328, TYR 326, PHE 343, and MET 436, with the bromine-substituted aromatic ring facilitating additional binding through van der Waals forces with residues like TYR 435, ILE 198, and LEU 171. **FBZ13** also forms hydrogen bonds with TYR 326, SER 59, and GLY 434, further stabilizing its binding, and engages polar residues such as GLN 206 and CYS
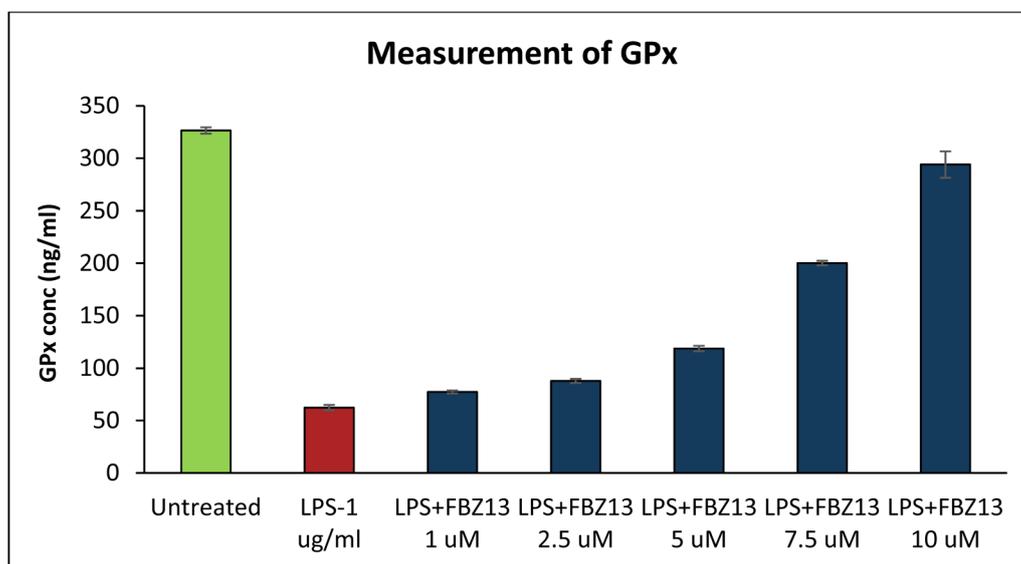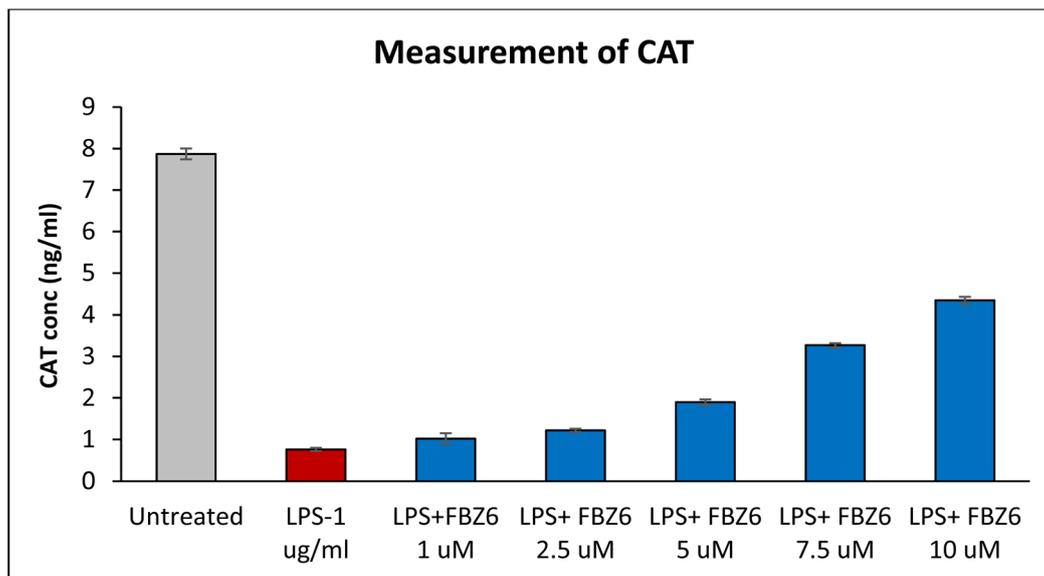
© 2025 The Author(s). Published by the Royal Society of Chemistry

(A)
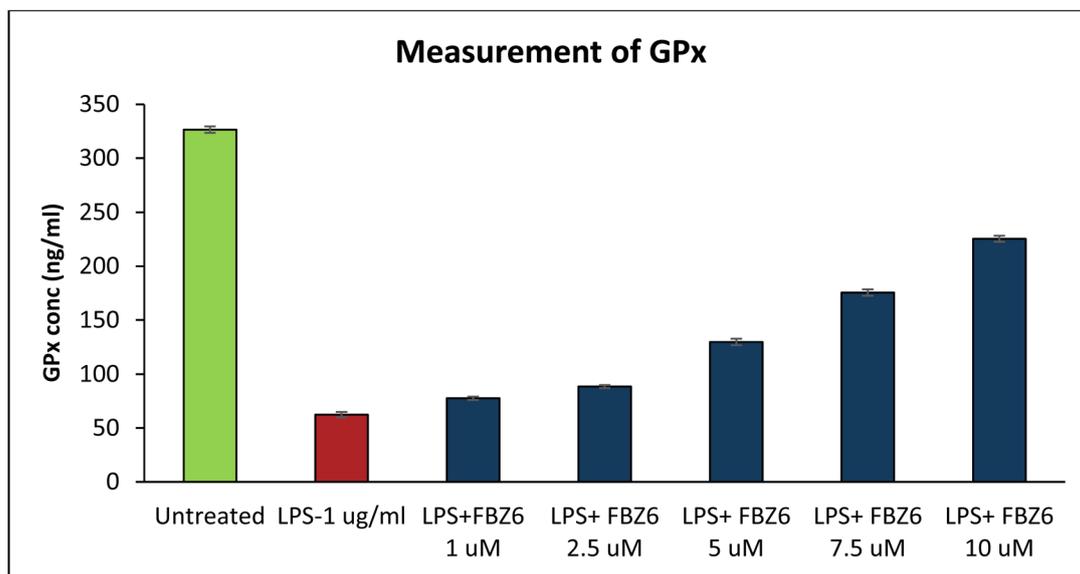
(B)

Fig. 7 GPx levels observed in untreated, LPS alone, different concentrations of **FBZ6** (A) and **FBZ13** (B) treatment against the LPS induced SH-SY5Y cells after the incubation period of 24 h. Each assay was performed in duplicate.

172. In addition to these interactions, **FBZ13** engages in strong π–π stacking with TYR 326 and PHE 343, contributing to a more stable binding conformation within the active site. Both compounds interact with key residues TYR 326, LEU 328, and PHE 343, essential for high binding affinity, but **FBZ13** demonstrates superior binding due to its additional interactions, including those with GLY 434 and TYR 435, and structural features like the bromine atom. This explains its slightly better docking score of -11.302 kcal mol^{-1} compared to **FBZ6** (-11.284 kcal mol^{-1}), consistent with its higher MAO-B inhibitory potency.

3.9. MD simulation

The MD simulation is used in drug development research for enabling the comprehension of energetic details about protein and ligand interactions in a time-affordable fashion, reproducing the nearly precise or realistic dynamic behaviour of a protein–ligand complex. In this study, all-atoms classical MD simulations were run for 100 ns on each complex to examine the binding stability at the atomic level and clarify the dynamic properties of the promising hit inhibitors inside the hMAO-B binding cavity. Various characteristics from the MD simulation trajectories, including protein backbone RMSD, RMSF, the
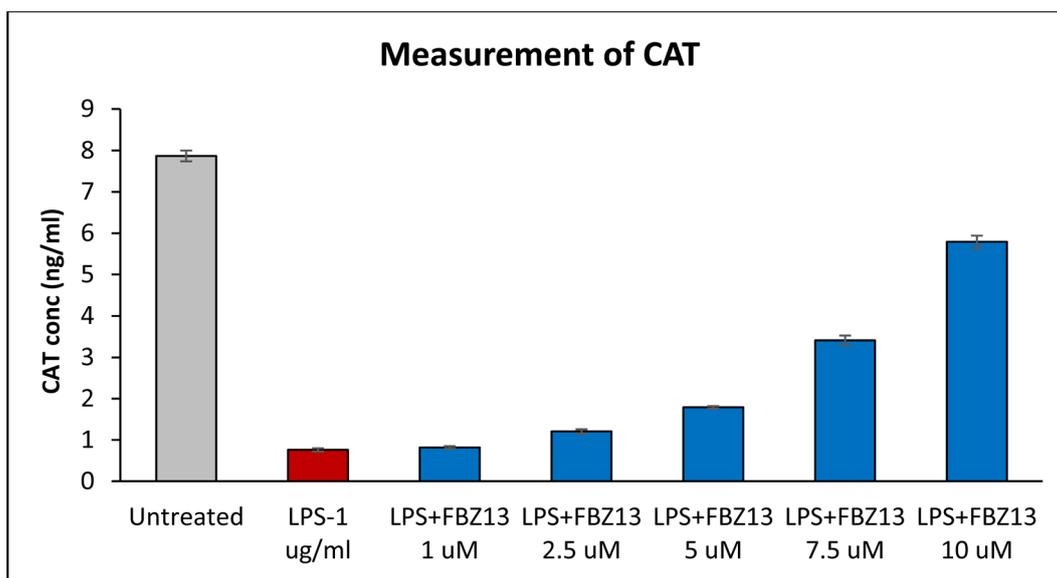
(B)

Fig. 8 CAT levels observed in untreated, LPS alone, different concentrations of **FBZ6** (A) and **FBZ13** (B) treatment against the LPS induced SH-SY5Y cells after the incubation period of 24 h. Each assay was performed in duplicate.

Table 3 XP docking scores of the lead compounds to the MAO-B active site

Compound	Docking score (kcal mol^{-1})
FBZ13	−11.302
FBZ6	−11.284
Safinamide	−12.671

radius of gyration (RGyr), PCA analysis, and binding free energy, were examined to assess the stability and flexibility of each protein–ligand complex.

3.9.1. Root-mean-square deviation (RMSD). The RMSD analysis of the **FBZ6** ligand–protein complex over 200 ns, depicted in Fig. 11 (A), provides insights into the structural dynamics of both the protein and the ligand. The protein RMSD, represented by the Cα backbone, shows an initial steady increase during the first 50 ns, indicative of structural relaxation and equilibration. Between 50 and 100 ns, the RMSD continues to rise, peaking around 3.0–3.5 Å, likely reflecting conformational flexibility or rearrangements in the protein backbone. After 100 ns, the protein RMSD stabilizes within the 2.8–3.5 Å range, suggesting that the protein has reached an equilibrium
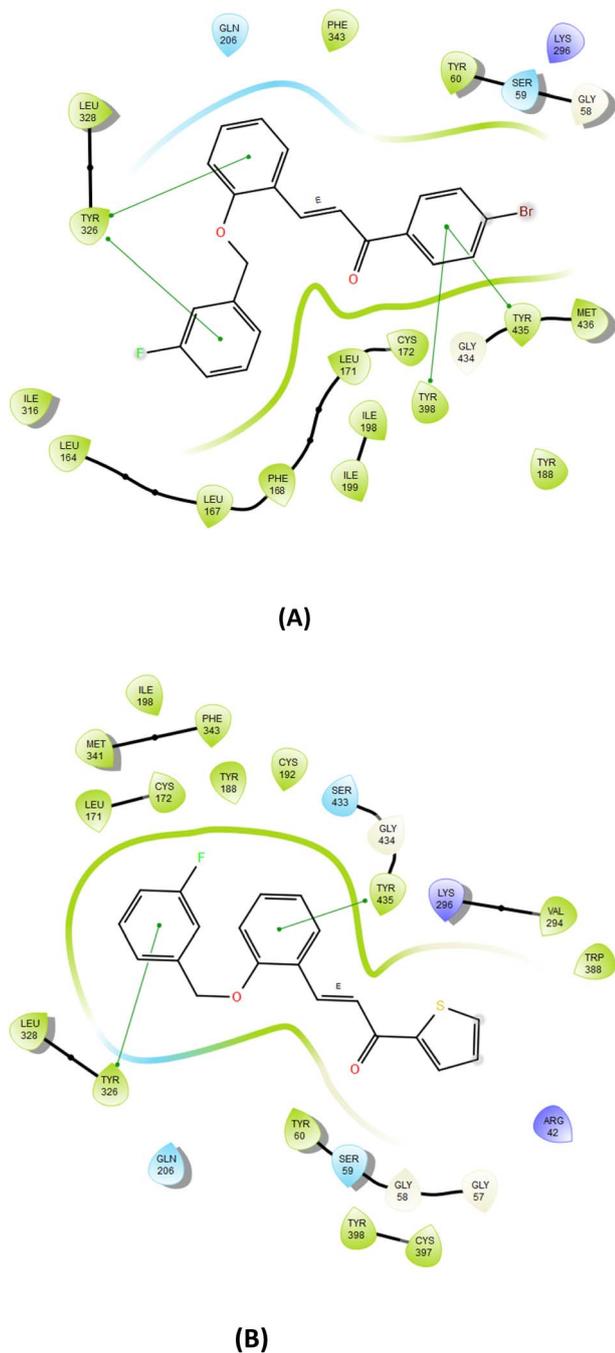
(A)

(B)

Fig. 9 Two-dimensional interaction of compound **FBZ13** (A) and **FBZ6** (B) to the active site of MAO-B (PDB ID: 2V5Z).

state with minimal large-scale structural fluctuations. In contrast, the ligand RMSD, calculated relative to the protein fit, starts with low values (<1.6 Å) during the initial 50 ns, indicating stable binding in its original position. A significant transition is observed between 50 and 75 ns, where the ligand RMSD rises sharply to approximately 4–5 Å, signalling a shift in the binding orientation or position of **FBZ6**. Beyond 75 ns, the ligand RMSD stabilizes around 4.5–5 Å, indicating that it adopts a new binding mode while maintaining stability, although slight

fluctuations suggest some flexibility in positioning within the binding pocket. By the end of the simulation, both the protein and ligand exhibit stable conformations, with the protein achieving structural stability and **FBZ6** displaying dynamic behaviour that transitions to a consistent binding conformation. These observations provide valuable information about the interaction and dynamics of **FBZ6** within the protein binding pocket.

The RMSD analysis of the **FBZ13** ligand–protein complex over 200 ns depicted in Fig. 11(B), provides detailed insights into the structural dynamics and stability of both the protein and the ligand. The protein RMSD (Cα backbone), depicted in blue, shows an initial increase during the first 50 ns, indicating structural equilibration and slight conformational adjustments. Following this phase, the protein RMSD stabilizes between 2.0 and 3.0 Å for the remainder of the simulation, suggesting that the protein achieves a relatively stable conformation with minimal large-scale fluctuations, indicative of a well-equilibrated protein structure. The ligand RMSD (pink curve), calculated relative to the protein fit, starts at values below 1.5 Å during the first 50 ns, signifying a tightly bound and stable initial binding mode. Unlike **FBZ6**, **FBZ13** exhibits a more restrained transition phase, with a gradual rather than abrupt increase in RMSD. After 50 ns, **FBZ13** stabilizes within the 2.0–2.5 Å range for the rest of the simulation, showing that the ligand maintains a consistent binding orientation with relatively minor positional or conformational adjustments. This stabilization reflects a strong and steady binding interaction between **FBZ13** and the protein binding pocket, with fewer fluctuations compared to **FBZ6**.

In comparison, **FBZ6** displayed a significantly different dynamic behaviour, with its ligand RMSD starting similarly stable but experiencing a sharp transition around 50–75 ns, where it rose to approximately 4.5–5.0 Å before stabilizing in a new binding mode. This suggests that **FBZ6** underwent a substantial reorientation or relocation within the binding pocket, settling into a different conformation with higher overall flexibility. **FBZ13**, in contrast, does not show such a dramatic shift, reflecting greater stability and potentially stronger or more favourable interactions within the binding site. The reduced RMSD values for **FBZ13** suggest less flexibility and greater fidelity to its initial binding conformation, which could indicate better binding affinity or a more optimal fit to the protein's binding pocket. These differences highlight the contrasting binding behaviour of the two ligands, with **FBZ13** exhibiting tighter and more consistent binding compared to the more dynamic behaviour of **FBZ6** (Fig. 11).

3.9.2. Root-mean-square fluctuation (RMSF). The analysis of the RMSF profiles for both **FBZ6** and **FBZ13** provides a comprehensive understanding of the residue-level flexibility and stability of the protein during the molecular dynamics simulations. The RMSF data reveal critical insights into the dynamic behaviour of the protein in response to the binding of these ligands, highlighting their similarities and differences in interaction and structural impact.

For both **FBZ6** and **FBZ13**, the RMSF profiles depicted in Fig. 12(A and B), indicate a generally stable protein structure,
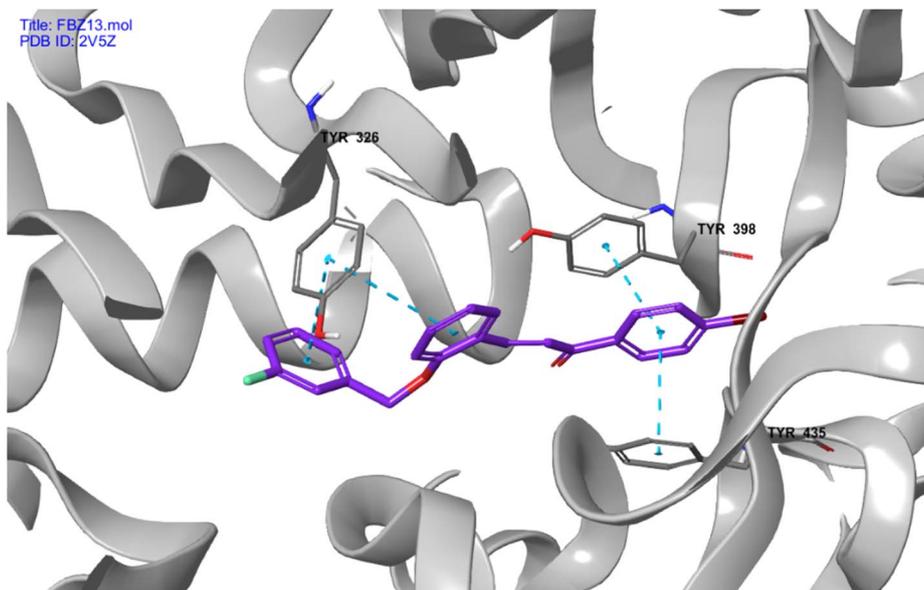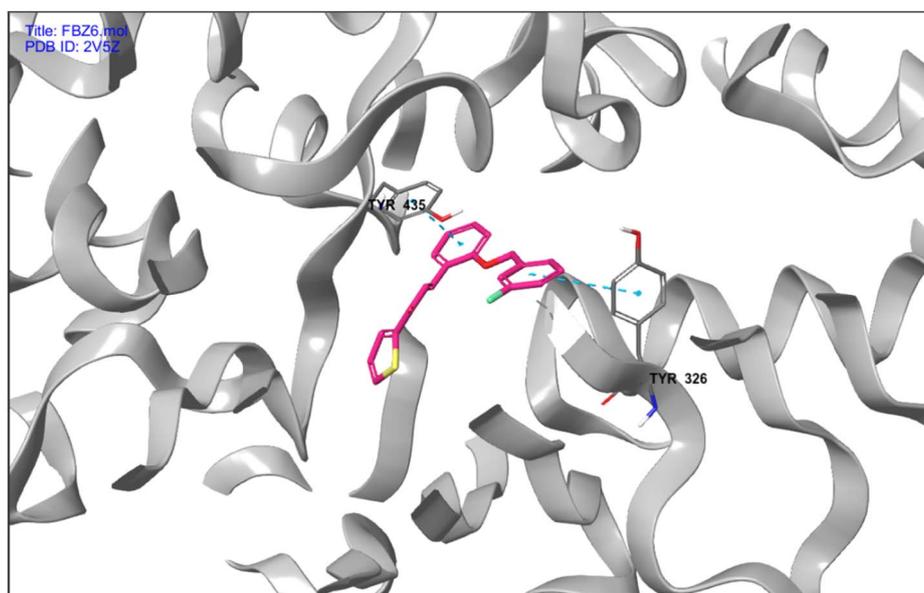
Fig. 10 Three-dimensional interaction of compound **FBZ13** (A) and **FBZ6** (B) to the active site of MAO-B (PDB ID: 2V5Z).

with most residues exhibiting low fluctuations below 1.5 Å. This stability is characteristic of the core regions of the protein, primarily composed of alpha-helices and beta-sheets, which maintain their rigidity due to strong intramolecular hydrogen bonds and hydrophobic interactions. The conserved stability across these core regions ensures the functional integrity of the protein throughout the simulation. However, notable

distinctions emerge in the regions of higher flexibility and their potential impact on ligand binding.

In the RMSF profile of **FBZ6**, regions around residue indices 90–110 and the terminal regions exhibit significant flexibility, with RMSF values exceeding 3 Å. These peaks correspond to loop regions and solvent-exposed residues, which inherently have greater mobility. The flexibility of these regions could
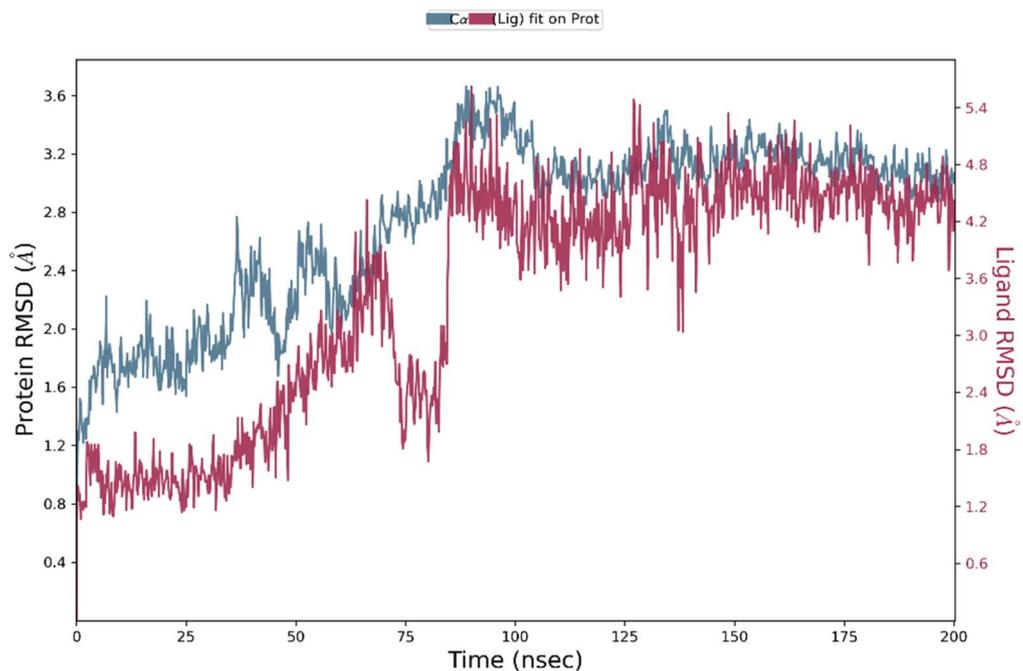
(A)
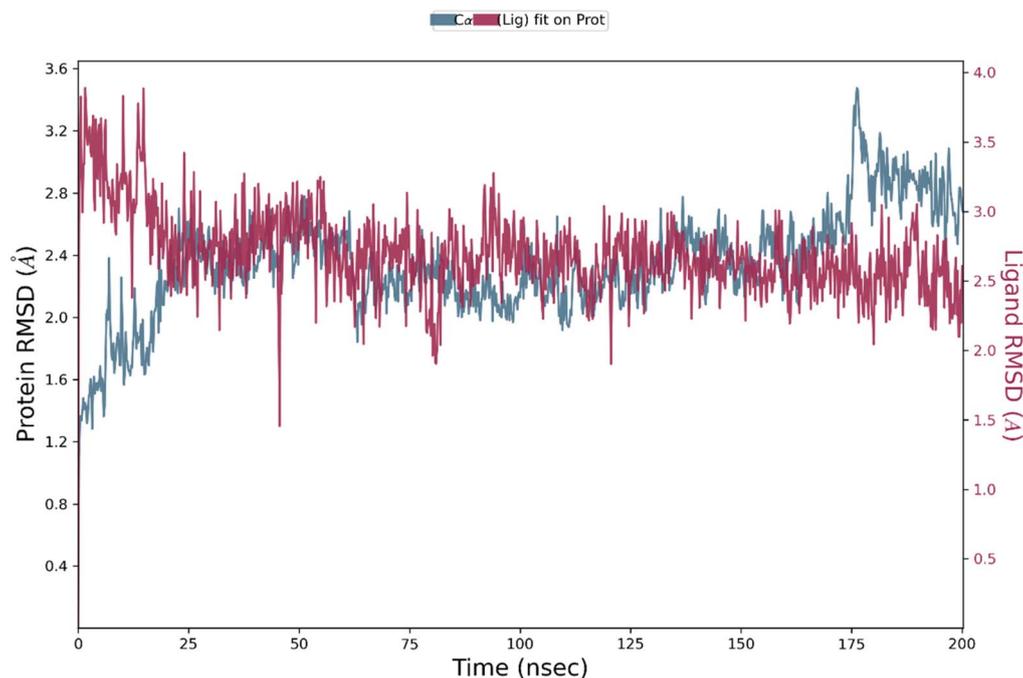
(B)

Fig. 11 RMSD of the time-dependent hMAO-B protein backbone with compounds **FBZ6** (A) and **FBZ13** (B) during 200 ns simulations.

facilitate ligand binding by allowing conformational adjustments in the protein structure. The C-terminal residues, in particular, show pronounced fluctuations, which is consistent with their typical behaviour as unconstrained regions.

Similarly, in the RMSF profile of **FBZ13**, peaks are observed around residue indices near 100 and in the terminal regions, with fluctuations surpassing 3 Å. These regions correspond to loop elements and solvent-exposed residues that contribute to
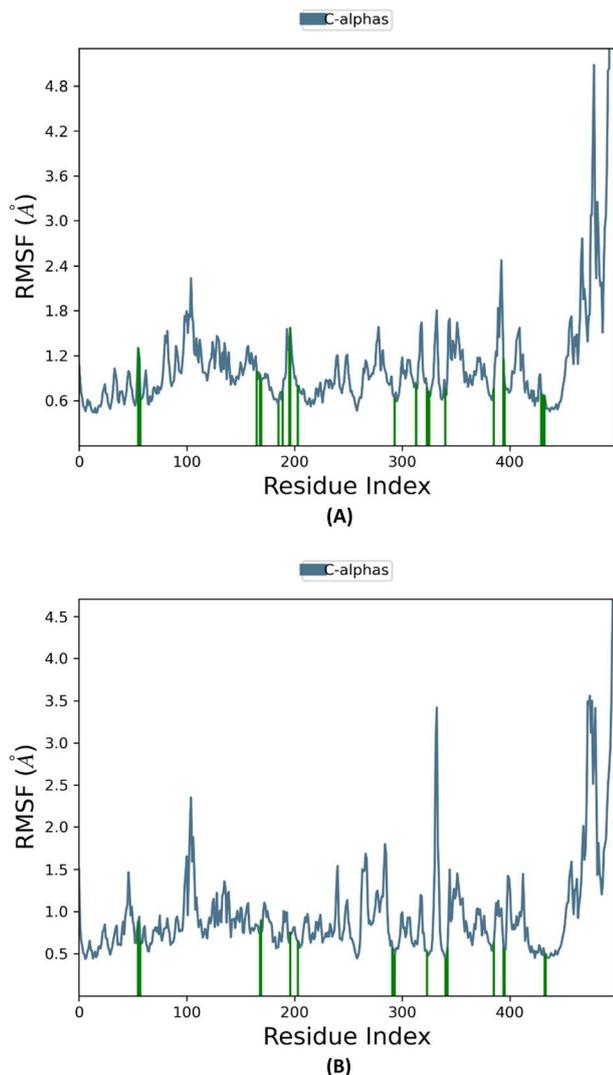
Fig. 12 RMSF of the hMAO-B protein backbone with compounds **FBZ6** (A) and **FBZ13** (B) during 200 ns simulations.

the dynamic nature of the protein. The heightened fluctuations at the C-terminal end are also evident, reflecting its characteristic mobility. The flexibility observed in both complexes underscores the role of these regions in supporting functional adaptability, such as accommodating ligand-induced structural changes or facilitating dynamic interactions within the binding pocket.

A key point of comparison lies in the binding pocket residues. For both **FBZ6** and **FBZ13**, these residues exhibit consistently low RMSF values, typically below 1 Å. This indicates high stability in the binding pocket, underscoring the robustness of the protein–ligand interactions. The residues directly involved in binding show minimal movement, highlighting their critical role in maintaining strong and stable interactions with the respective ligands. This stability is crucial for ensuring the efficacy of both **FBZ6** and **FBZ13** as inhibitors, as it preserves the structural integrity of the binding pocket and enhances ligand affinity.

Despite these similarities, subtle differences in the RMSF profiles of the two complexes suggest variations in their dynamic behaviour. For instance, **FBZ6** appears to induce slightly higher fluctuations in certain loop regions compared to **FBZ13**. This could indicate differences in how each ligand interacts with the protein and induces localized conformational changes. **FBZ13**, on the other hand, appears to stabilize the protein–ligand complex slightly more effectively, as reflected in the lower overall fluctuations in the binding pocket residues. This suggests that **FBZ13** may form stronger or more consistent interactions with the binding site compared to **FBZ6**.

Both ligands exhibit a balance between rigidity and flexibility in the protein structure. The low fluctuations in the binding pocket residues ensure strong and stable ligand interactions, while the flexibility in loop and solvent-exposed regions supports the dynamic requirements of the binding process. However, **FBZ13** demonstrates a marginally greater ability to stabilize the protein, potentially contributing to its enhanced binding affinity and inhibitory activity.

The RMSF analyses of **FBZ6** and **FBZ13** highlight the dynamic nature of protein–ligand interactions, emphasizing the importance of specific residues in stabilizing the complexes while allowing functional adaptability. While both ligands effectively stabilize the binding pocket and maintain the structural integrity of the protein, **FBZ13** shows slightly enhanced stabilization compared to **FBZ6**. These findings provide valuable insights into the molecular mechanisms underlying the interactions of **FBZ6** and **FBZ13** with the protein, offering a deeper understanding of their structural and functional implications (Fig. 12).

4 Conclusion

In this study, thirteen fluorobenzyloxy chalcone derivatives were synthesized and evaluated for their MAO inhibitory activity. All compounds exhibited greater selectivity for MAO-B over MAO-A, with **FBZ13** emerging as the most potent MAO-B inhibitor (IC$_{50}$ = 0.0053 μM), surpassing the reference inhibitor safinamide. **FBZ13** and **FBZ6** demonstrated the highest selectivity indices, indicating their strong preference for MAO-B. Kinetic studies confirmed that both compounds act as competitive reversible inhibitors, with **FBZ13** displaying superior binding affinity. Additionally, PAMPA assay results suggested that these lead compounds possess favorable CNS permeability. Furthermore, *in vitro* antioxidant assays revealed that **FBZ13** and **FBZ6** effectively mitigated LPS-induced oxidative stress by enhancing antioxidant enzyme activities, with **FBZ13** exhibiting superior efficacy. Molecular docking studies further validated their strong binding interactions with hMAO-B, primarily through π–π stacking, reinforcing their potential as therapeutic candidates. Overall, the findings suggest that **FBZ6** and **FBZ13** are promising selective MAO-B inhibitors with significant neuroprotective properties. Their potent inhibitory activity, coupled with strong antioxidant effects and favourable pharmacokinetic profiles, highlights their potential as lead candidates for the treatment of neurodegenerative disorders such as Parkinson's and Alzheimer's diseases. Despite demonstrating potent *in vitro*

MAO-B inhibitory activity and favourable permeability profiles, the current study on fluorinated benzyloxybenzene–chalcone derivatives lacks *in vivo* validation and detailed toxicity assessments; therefore, future studies must evaluate their pharmacokinetic properties, brain penetration, and safety profile in animal models to better assess their therapeutic potential for neurodegenerative diseases.

Conflicts of interest

There are no conflicts to declare.

Data availability

The data supporting this article have been included as part of the supplementary information (SI). Supplementary information is available. See DOI: **https://doi.org/10.1039/d5ra06971h**.

Acknowledgements

References

1 L. V. Kalia and A. E. Lang, *Lancet*, 2015, **386**, 896–912.

2 W. Poewe, *Nat. Rev. Dis. Primers*, 2020, **6**, 1–2.

3 A. H. V. Schapira, K. R. Chaudhuri and P. Jenner, *Nat. Rev. Neurosci.*, 2017, **18**, 435–450.

4 A. J. Espay, L. V. Kalia, Z. Gan-Or, C. H. Williams-Gray, P. L. Bedard, S. M. Rowe, F. Morgante, A. Fasano, B. Stecher, M. A. Kauffman, M. J. Farrer, C. S. Coffey, M. A. Schwarzschild, T. Sherer, R. B. Postuma, A. P. Strafella, A. B. Singleton, R. A. Barker, K. Kieburtz, C. W. Olanow, A. Lozano, J. H. Kordower, J. M. Cedarbaum, P. Brundin, D. G. Standaert and A. E. Lang, *Neurology*, 2020, **94**, 481.

5 R. Arya, A. K. M. A. Haque, H. Shakya, M. M. Billah, A. Parvin, M. M. Rahman, K. M. Sakib, H. M. Faruquee, V. Kumar and J. J. Kim, *Int. J. Mol. Sci.*, 2024, **25**, 12379.

6 G. Höglinger, C. Trenkwalder and M. Bähr, *Neurol. Res. Practice*, 2024, **6**, 30.

7 A. N. MacMahon Copas, S. F. McComish, J. M. Fletcher and M. A. Caldwell, *Front. Neurol.*, 2021, **12**, 666737.

8 S. Bindra, A. Datta, H. Khader, A. Yasin, R. R. Thomas, S. Verma, A. Patel, D. Grace, T. Parambi, S. N. Mali, T. M. Rangarajan and B. Mathew, *ACS Omega*, 2024, **9**, 44005–44018.

9 C. M. Tanner and J. L. Ostrem, *N. Engl. J. Med.*, 2024, **391**, 442–452.

10 L. Dezsi and L. Vecsei, *CNS Neurol. Disord.: Drug Targets*, 2017, **16**, 425–439.

11 G. S. Baweja, S. Gupta, B. Kumar, P. Patel and V. Asati, *Mol. Divers.*, 2024, **28**, 1823–1845.

12 F. Chimenti, R. Fioravanti, A. Bolasco, P. Chimenti, D. Secci, F. Rossi, M. Yáñez, F. Orallo, F. Ortuso and S. Alcaro, *J. Med. Chem.*, 2009, **52**, 2818–2824.

13 D. Kar Mahapatra, V. Asati and S. K. Bharti, *Expert Opin. Ther. Pat.*, 2019, **29**, 385–406.

14 P. Riederer and T. Müller, *J. Neural Transm.*, 2018, **125**, 1751–1757.

15 E. Mateev, M. Georgieva, A. Mateeva, A. Zlatkov, S. Ahmad, K. Raza, V. Azevedo and D. Barh, *Molecules*, 2023, **28**, 4814.

16 B. R. Bloem, M. S. Okun and C. Klein, *Lancet*, 2021, **397**, 2284–2303.

17 A. Lees, E. Tolosa, F. Stocchi, J. J. Ferreira, O. Rascol, A. Antonini and W. Poewe, *Expert Rev. Neurother.*, 2023, **23**, 15–24.

18 G. Abbruzzese, P. Barone, L. Lopiano and F. Stocchi, *Drug Des., Dev. Ther.*, 2021, **15**, 2507–2517.

19 H. Wasan, D. Singh and R. KH, *Brain Res. Bull.*, 2021, **168**, 165–177.

20 I. A. Lillethorup, A. V. Hemmingsen and K. Qvortrup, *RSC Med. Chem.*, 2025, **16**, 1037–1048.

21 K. J. Hodgetts, K. J. Combs, A. M. Elder and G. C. Harriman, *Annu. Rep. Med. Chem.*, 2010, **45**, 429–448.

22 M. N. Kumar, S. L. Nargund Professor, C. Author and S. L. Nargund, *Int. J. Pharm. Pharmaceut. Sci.*, 2025, **7**, 154–160.

23 P. Guglielmi, B. Mathew, D. Secci and S. Carradori, *Eur. J. Med. Chem.*, 2020, **205**, 112650.

24 W. Li, J. Huang, Z. Chen, D. Zhang, L. He, Y. Guo, L. Zhong, C. Yang, C. Yang, M. Zeng, J. Zhu and Z. Cao, *Curr. Med. Chem.*, 2025, **33**, 351–368.

25 J. W. Choi, B. K. Jang, N. C. Cho, J. H. Park, S. K. Yeon, E. J. Ju, Y. S. Lee, G. Han, A. N. Pae, D. J. Kim and K. D. Park, *Bioorg. Med. Chem.*, 2015, **23**, 6486–6496.

26 S. T. Sudevan, J. M. Oh, M. A. Abdelgawad, M. A. S. Abourehab, T. M. Rangarajan, S. Kumar, I. Ahmad, H. Patel, H. Kim and B. Mathew, *Sci. Rep.*, 2022, **12**, 1–19.

27 A. K. Singh, S. M. Kim, J. M. Oh, M. A. Abdelgawad, M. M. Ghoneim, T. M. Rangarajan, S. Kumar, S. T. Sudevan, D. Trisciuzzi, O. Nicolotti, H. Kim and B. Mathew, *Chem. Biol. Drug Des.*, 2023, **102**, 271–284.

28 N. Chandran, J. Lee, P. Prabhakaran, S. Kumar, S. T. Sudevan, D. G. T. Parambi, T. G. Alsahli, M. Pant, H. Kim and B. Mathew, *Sci. Rep.*, 2024, **14**, 1–17.

29 S. Kumar, J. M. Oh, M. A. Abdelgawad, M. A. S. Abourehab, A. K. Tengli, A. K. Singh, I. Ahmad, H. Patel, B. Mathew and H. Kim, *ACS Omega*, 2023, **8**, 6908–6917.

30 D. Choudhary, B. Kumar, B. Chandrasekaran, T. G. Singh, R. Kaur, A. Aldahish, R. Vasudevan and P. Balaji, *Pharmaceuticals*, 2025, **18**, 309.

31 Z. Wang, C. Yi, K. Chen, T. Wang, K. Deng, C. Jin and G. Hao, *Eur. J. Med. Chem.*, 2022, **228**, 114025.

32 C. Yi, X. Liu, K. Chen, H. Liang and C. Jin, *Eur. J. Med. Chem.*, 2023, **252**, 115308.

33 J. I. Castillo-Arellano, Z. Stryker, M. D. Wyatt and F. León, *ACS Med. Chem. Lett.*, 2024, **15**, 610–618.

34 A. Asim, M. K. Jastrzębski and A. A. Kaczor, *Molecules*, 2025, **30**, 2975.

35 A. Elkamhawy, J. M. Oh, M. Kim, L. O. El-Halaby, M. H. Abdellattif, A. A. Al-Karmalawy, H. Kim and K. Lee, *Mol. Divers.*, 2024, 1–15.

36 J. M. Oh, H. J. Jang, M. G. Kang, S. K. Mun, D. Park, S. J. Hong, M. H. Kim, S. Y. Kim, S. T. Yee and H. Kim, *Molecules*, 2023, **28**, 258.

37 A. K. El-Damasy, J. M. Oh, H. J. Kim, S. K. Mun, A. A. Al-Karmalawy, R. Alnajjar, Y. J. Choi, J. J. Kim, G. Nam, H. Kim and G. Keum, *Bioorg. Chem.*, 2024, **142**, 106939.

38 J. M. Oh, Q. Gao, W. H. Shin, E. Y. Lee, D. Chung, G. Choi, S. J. Nam and H. Kim, *Appl. Biol. Chem.*, 2024, **67**, 1–12.

39 M. Radan, T. Djikic, D. Obradovic and K. Nikolic, *Eur. J. Pharm. Sci.*, 2022, **168**, 106056.

40 J. R. Dominguez-Rodriguez, P. C. Gomez-Contreras, G. Hernandez-Flores, J. M. Lerma-Diaz, A. Carranco, R. Cervantes-Munguia, S. Orbach-Arbouys and A. Bravo-Cuellar, *Anticancer Res.*, 2001, **21**, 1869–1872.

41 I. Engelbrecht, S. Horn, J. P. Giesy and R. Pieters, *MethodsX*, 2023, **11**, 102395.

42 B. Halliwell and J. M. C. Gutteridge, *Free Radicals in Biology and Medicine*, Oxford University Press, 2015.

43 A. Ricci, S. Zara, V. di Giacomo, M. Gallorini, M. Rapino, N. Di Pietro, A. Cipollina, A. Piattelli and A. Cataldi, *Int. J. Mol. Sci.*, 2025, **26**, 8600.

44 I. Engelbrecht, S. Horn, J. P. Giesy and R. Pieters, *MethodsX*, 2023, **11**, 102395.

45 S. Anwar, T. Sarwar, A. A. Khan and A. H. Rahmani, *Biomolecules*, 2025, **15**, 1130.

46 M. H. Hadwan, A. Hassan Alta'ee, R. M. Mohammed, A. M. Hadwan, H. S. Al-Kawaz, Z. Abbas and A. Talebi, *Bull. Natl. Res. Cent.*, 2024, **48**, 1–14.

47 Y. O. Ayipo, S. N. Yahaya, H. F. Babamale, I. Ahmad, H. Patel and M. N. Mordi, *Turk. J. Biol.*, 2021, **45**, 503–517.

48 A. Malani, A. Makwana, J. Monapara, I. Ahmad, H. Patel and N. Desai, *J. Biochem. Mol. Toxicol.*, 2021, **35**, e22903.

49 S. Kumar, J. M. Oh, M. A. Abdelgawad, M. A. S. Abourehab, A. K. Tengli, A. K. Singh, I. Ahmad, H. Patel, B. Mathew and H. Kim, *ACS Omega*, 2023, **8**, 6908–6917.

50 S. S. Kapale, S. N. Mali and H. K. Chaudhari, *Med. Drug Discovery*, 2019, **2**, 100008.

51 S. N. Mali, A. Pandey, R. R. Bhandare and A. B. Shaik, *Sci. Rep.*, 2022, **12**, 1–21.

52 M. Asadi, M. Ebrahimi, M. Mohammadi-Khanaposhtani, H. Azizian, S. Sepehri, H. Nadri, M. Biglar, M. Amanlou, B. Larijani, R. Mirzazadeh, N. Edraki and M. Mahdavi, *Chem. Biodivers.*, 2019, **16**, e1900370.

53 F. A. D. M. Opo, M. M. Rahman, F. Ahammad, I. Ahmed, M. A. Bhuiyan and A. M. Asiri, *Sci. Rep.*, 2021, **11**, 4049.

54 M. Shah, S. Bashir, S. Jaan, H. Nawaz, U. Nishan, S. W. Abbasi, S. B. Jamal, A. Khan, S. G. Afridi and A. Iqbal, *South Afr. J. Bot.*, 2021, **143**, 462–473.

55 M. Shah, S. Jaan, B. Fatima, M. S. Javed, A. Amjad, A. Khan, S. G. Afridi, U. Nishan, A. Iqbal and H. Nawaz, *Int. J. Pept. Res. Ther.*, 2021, **27**, 181–195.

56 S. Jaan, M. Shah, N. Ullah, A. Amjad, M. S. Javed, U. Nishan, G. Mustafa, H. Nawaz, S. Ahmed and S. C. Ojha, *Front. Microbiol.*, 2022, **13**, 971263.

57 G. Kanagaraju and A. Thangamani, *Res. J. Chem. Sci.*, 2014, **4**, 23–31.

58 G. B. Souza, T. A. C. Santos, A. P. S. Silva, A. L. B. S. Barreiros, V. B. Nardelli, I. B. Siqueira, S. S. Dolabella, E. V. Costa, P. B. Alves, R. Scher and R. P. M. Fernandes, *Nat. Prod. Res.*, 2024, **38**, 1326–1333.

59 D. G. Thomas Parambi, J. M. Oh, S. Kumar, S. T. Sudevan, O. M. Hendawy, M. A. Abdelgawad, A. Musa, M. M. Al-Sanea, I. Ahmad, H. Patel, H. Kim and B. Mathew, *Comput. Biol. Chem.*, 2023, **105**, 107899.

60 A. Krishna, J. Lee, S. Kumar, S. T. Sudevan, P. Uniyal, L. K. Pappachen, H. Kim and B. Mathew, *Appl. Biol. Chem.*, 2023, **66**, 1–10.

61 D. G. T. Parambi, J. M. Oh, S. C. Baek, J. P. Lee, A. R. Tondo, O. Nicolotti, H. Kim and B. Mathew, *Bioorg. Chem.*, 2019, **93**, 103335.

62 B. Mathew, J. M. Oh, M. A. Abdelgawad, A. Khames, M. M. Ghoneim, S. Kumar, L. R. Nath, S. T. Sudevan, D. G. T. Parambi, C. Agoni, M. E. S. Soliman and H. Kim, *ACS Omega*, 2022, **7**, 8184–8197.

63 B. Mathew, J. M. Oh, A. Khames, M. A. Abdelgawad, T. M. Rangarajan, L. R. Nath, C. Agoni, M. E. S. Soliman, G. E. Mathew and H. Kim, *Pharmaceuticals*, 2021, **14**, 1148.

64 N. A. Rehuman, J. M. Oh, M. A. Abdelgawad, E. A. M. Beshr, M. A. S. Abourehab, N. Gambacorta, O. Nicolotti, R. K. Jat, H. Kim and B. Mathew, *Pharmaceuticals*, 2022, **15**, 1152.

65 B. Mathew, J. M. Oh, R. S. Baty, G. E. S. Batiha, D. G. T. Parambi, N. Gambacorta, O. Nicolotti and H. Kim, *Environ. Sci. Pollut. Res. Int.*, 2021, **28**, 38855.

66 A. K. El-Damasy, J. E. Park, H. J. Kim, J. Lee, E. K. Bang, H. Kim and G. Keum, *Pharmaceuticals*, 2023, **16**, 83.